

Marek Sebastian Simon

Benchmark and Validation of non-linear EIRENE Monte Carlo neutral transport solver

**IPP 17/28
Mai, 2011**

Ludwig-Maximilians-Universität München



Benchmark and Validation of non-linear EIRENE Monte Carlo neutral transport solver

Marek Sebastian Simon

May 31, 2011

DIPLOMA THESIS PERFORMED AT THE
Max-Planck-Institut für Plasmaphysik (IPP), Garching



Erstgutachter: Prof. Dr. Hartmut Zohm

Zweitgutachter: Prof. Dr. Harald Lesch

Abstract

Determination of neutral particle distributions, is of great interest for the design of a fusion reactor. Unfortunately in a fusion reactor the neutral particle densities present, give rise to a collisionality where collisions can not be neglected but fluid descriptions fail as well. Therefore massive computational effort is required for solving the Boltzmann equation with a nonlinear collision integral. The Monte Carlo linear transport solver EIRENE represents a possibility to solve the Boltzmann equation in the BGK approximation, while being inherently parallelizable. In this thesis, the calculation of particle distributions has been validated and benchmarked by comparing conductances calculated by EIRENE with well documented cases in the literature. Conductances were calculated for rectangular orifices, tubes of different length, as well as at different pressure ratios. The agreement was found to be very good for $Kn > 0.1$ and for some cases even $Kn > 0.01$. In addition the existing code was extended to include a more realistic approximation of the collision integral and a first qualitative validation was performed.

Contents

1	Introduction	1
1.1	Nuclear Fusion	1
1.2	The Tokamak principle	2
1.3	ASDEX Upgrade and Divertor concept	3
1.4	Motivation of this Thesis	6
2	Basic Concepts in Vacuum Physics	8
2.1	Conductance	8
2.2	Knudsen Number	9
2.3	Flow-Regimes	10
2.4	Calculation of conductance in the free-molecular or Knudsen regime and the concept of transmission probability	11
2.5	Calculation of conductance in the transition-flow-regime	13
2.6	Calculation of conductance in the continuum-flow-regime	14
3	Kinetic Equations and Monte Carlo Simulations	16
3.1	The single species Boltzmann Equation	16
3.2	Treatment of the Boltzmann Collision Integral	18
3.3	The BGK approximation	20
3.4	The ellipsoidal BGK approximation for correct Prandtl number	21
3.5	Implemented Transformation	22
3.6	EIRENE - BGK/BGKES	23
3.6.1	Sampling Free Path:	23
3.6.2	Collision - Sampling	24
3.6.3	Successive Linearization Method	24
3.6.4	Responses	24
3.6.5	Statistical Error	25
4	Grid Generation and Methods of Evaluation	26
4.1	The EIRENE Input-file	26
4.1.1	Input Block 1: Input data for operating mode	26
4.1.2	Input Block 2: Input data for standard mesh	26
4.1.3	Input Block 3A: Non-default Standard Surfaces	27
4.1.4	Input Block 3B: Additional surfaces	27

4.1.5	Input Block 7: Input data for Initial Distribution of Test Particles	27
4.2	General geometrical set-up	28
4.3	Grids with aperture of rectangular cross-section	29
4.3.1	Grid for slit created by 2D-triangular mesh for free molecular length scan	29
4.3.2	Grid for slit created by 2D-triangular mesh for Knudsen-scan	29
4.3.3	Grid for slit created by 3D cartesian mesh	32
4.4	Grids with apertures of circular cross-section	33
4.4.1	Grid for tube of finite length with circular cross-section generated by a rotated 2D cartesian mesh	33
4.4.2	Grid for circular orifice generated by a 3D-Cartesian with an additional surface	35
4.4.3	Grid for a circular orifice generated by a rotated 2D triangular mesh	36
4.5	Comparison between grid performance	37
4.6	Uncertainties	39
4.6.1	Convergence	39
4.6.2	Statistical error	40
4.6.3	Influence of the grid	40
5	Results	42
5.1	Free molecular length scan of a slit	42
5.2	Knudsen scan of a slit	43
5.3	Knudsen scan of a circular orifice	45
5.4	Circular Pipe: Lengthscan	46
5.5	Conductance at finite pressure ratios	46
5.6	The BGKES extension	51
6	Summary and Conclusion	54
7	Appendix	56
7.1	Table for parameters in Fujimoto Usami formula	56
7.2	Example of formatted Input-File	57
7.3	Implemented Code	62

Chapter 1

Introduction

Finding a safe, economical and ecologically sustainable source of energy is crucial in meeting the challenges of the 21st century. Increasing population and the scarcity of conventional energy resources, as well as environmental and political issues, call for the investigation and development of alternative energy concepts. Among others, energy from nuclear fusion has been identified as a promising candidate to meet most criteria for a potential future energy source. As an international effort, the first experiment, expected to answer the question of feasibility of nuclear fusion as an energy source, is ITER, which is currently being built in Cadarache, France. The following chapter will give a rough overview over the principles of nuclear fusion, the tokamak as well as ASDEX Upgrade and the divertor concept and finally motivate the topic of this thesis.

1.1 Nuclear Fusion

Fusion is the process of two or more nuclei approximating within reach of the strong force ($\approx 10^{-15}m$) and consequently sticking together. If the binding energy of the product is larger than the sum of binding energy of the reactants, the process is exo-thermal and releases energy. Notice in Fig 1.1 the large gap in binding energy for helium, resulting from the Pauli spin-exclusion principle, with the helium spin-configuration being particularly favorable.

Unfortunately, bringing two nuclei as close together as to reach coupling with the strong force is not trivial. Having the lowest charge, hydrogen H and the hydrogen isotopes deuterium D and tritium T are least affected by Coulomb repulsion, so most fusion reactions considered for energy production involve fusion from hydrogen nuclei to helium. The most important is:



For temperatures around 10-20keV, and considering quantum tunneling effects, the ratio of fast particles overcoming the Coulomb barrier is large enough as to allow for significant reaction cross-sections $\langle\sigma\rangle$. At these temperatures almost all

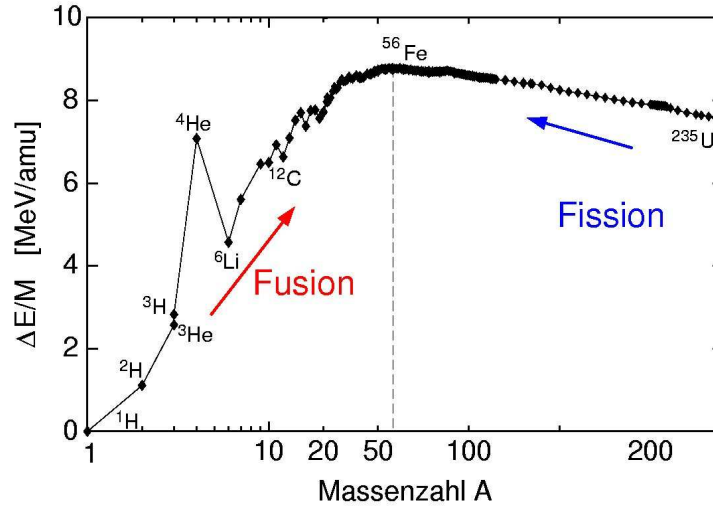


Figure 1.1: Binding energy pro nucleon. Iron, having the maximum binding energy and therefore the most stable nucleus, is marked.

hydrogen-atoms are ionized and form a plasma state. In order to allow for reaction rates $n_D n_T \langle \sigma v \rangle$ of a confined plasma where the energy produced is sufficient to overcome losses, densities have to be exceeded while maintaining high temperatures. With the energy confinement time τ_E a measure for thermal insulation, this relationship is expressed by the Lawson criterion, stating the ignition threshold in terms of the triple product (*density \times temperature \times energy confinement time*) [1]:

$$n_e T \tau_E \geq 2.8 \cdot 10^{21} \text{keV cm}^{-3} \quad (1.2)$$

To reach these conditions, different methods of confinement have been investigated. One is magnetic confinement and so far, two promising configurations, the stellarator and the tokamak, have been found. At IPP, research is performed on both concepts, namely the stellarator W-7X at IPP Greifswald and the tokamak ASDEX Upgrade at IPP Garching.

1.2 The Tokamak principle

Plasmas, being ionized and therefore reacting to electromagnetic forces, can be confined by magnetic fields. For linear configurations, confinement at the ends, is very weak and the losses of particles and energy are too large, so toroidal systems have been developed. Unfortunately because of the toroidal shape, the magnetic field is inhomogeneous, giving rise to opposed drifts ($\nabla \mathbf{B}$ -drift and $\nabla \times \mathbf{B}$ -drift) in electrons

and ions and therefore charge separation. The resulting electric field induces an additional $\mathbf{E} \times \mathbf{B}$ -drift that ultimately drives all charged-particles outward, causing fast radial losses (see Fig. 1.2). These losses can be eliminated by the superposition of a poloidal magnetic field, compensating the effects of the $\nabla \mathbf{B}$ -drift and $\nabla \times \mathbf{B}$ -drift by a rotation around the poloidal axis [2]. This configuration is called the tokamak (acronym for "*toroidalnaya kamera aksial'nyy magnitnyy polem*", translated from Russian: "toroidal chamber with axial magnetic field") and was invented by the Russian physicists Tamm and Sakharov in 1952[1].

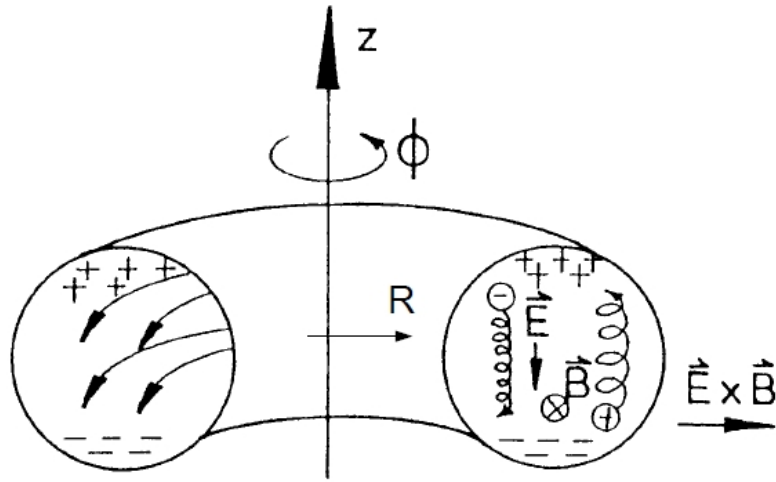


Figure 1.2: Toroidal plasma configuration with drifts, causing charge separation and therefore radial losses

In a tokamak, the toroidal component of the magnetic field is generated by magnetic coils, while the poloidal component is generated by inducing a toroidal plasma current, which also serves to heat and ionize the plasma fuel. Although this is the basic concept of a tokamak already, many more subtleties of the complex behavior of the confined plasma, like MHD-instabilities or collisional and turbulent transport, have to be considered, as well, in order to produce a stable plasma for a fusion power plant.

1.3 ASDEX Upgrade and Divertor concept

The goal of the ASDEX ("Axialsymmetric Divertor Experiment") Upgrade in Garching is to investigate crucial problems in fusion research under reactor-like conditions. The major contributions, among many others, resulting from ASDEX Upgrade and its predecessor ASDEX involve the development of a high confinement scenario, the so called "H-mode", the exploration of plasma-wall interactions,

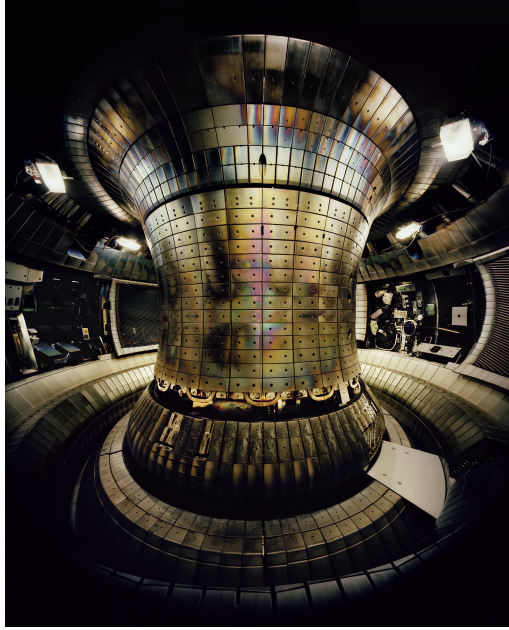


Figure 1.3: Inside view of the ASDEX Upgrade vacuum vessel

particularly using the concept of a Divertor, and only recently, the use of resonant magnetic perturbation coils to suppress energy loss from edge localized mode (ELM) instabilities. Because this thesis is in particular concerned with distributions of neutral particles, I will first give a brief overview of the Divertor concept and the role neutral particles play in the vessel:

Maintaining a sufficient density of the reactants is critical to fulfill the Lawson criterion (Eq. 1.2). For that purpose, fuel in the form of neutral particles has to be injected to increase the ion-density in the plasma core n_i . Furthermore the fusion "exhaust", i.e. the helium-"ash" and other impurities, which otherwise dilute the concentration of the fuel reactants and reduce the temperature due to enhanced radiation loss, have to be removed. To leave the magnetic confinement, the helium ash needs to become neutralized by interaction with the walls. Plasma-wall interactions can only take place at the plasma edge where temperatures are low enough for the wall-material to endure. The neutral helium can then be extracted by pumps. In turn, high pumping efficiencies require high neutral pressures in the region in front of the pumping duct. A low temperature, high density region at the plasma boundary can be achieved in a tokamak in the so called Divertor [3].

In a Divertor configuration the magnetic flux surfaces are formed to create an X-point where the poloidal field vanishes. The magnetic flux surface crossing this X-point is called the *Separatrix*, which is also the *Last Closed Flux Surface* (LCFS) and any surface outside the Separatrix is part of the so called Scrape Off Layer (SOL) (see Fig 1.4) where magnetic flux surfaces are not closed anymore. All particle,

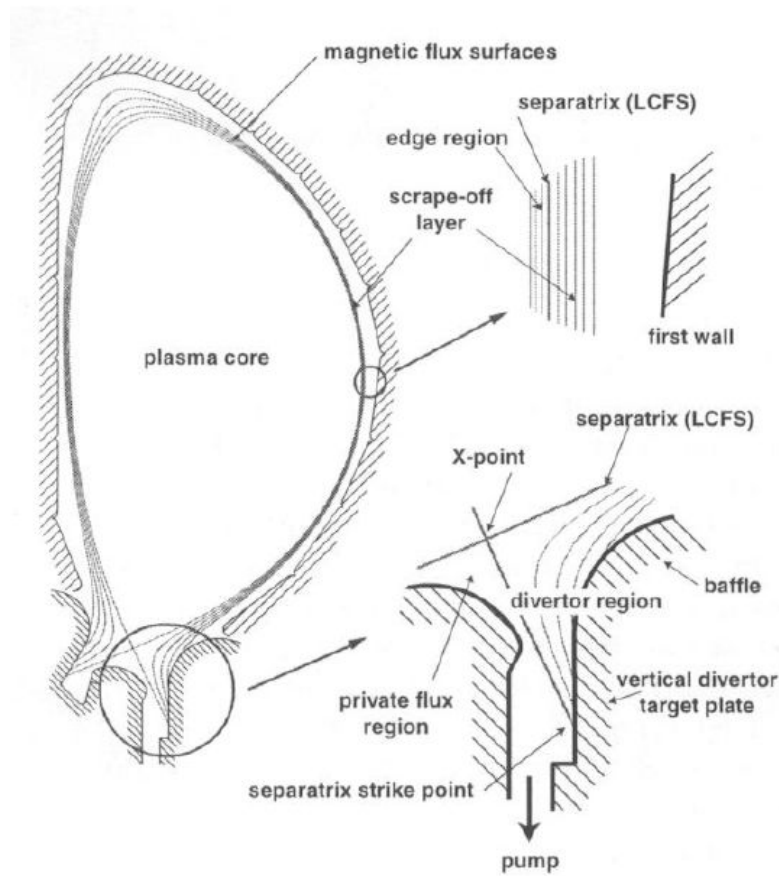


Figure 1.4: Schematic view of the plasma vessel. The Separatrix separates the plasma from the SOL and leads the LCFS to the Divertor, which is designed as an intentional point of plasma-wall interaction. Through the recycling high concentrations of neutral particles are generated and the pumping efficiency is increased to remove helium and other impurities

momentum and energy emission from the LCFS is guided towards the points where the Separatrix and the other SOL field lines strike the wall below the X-point. The Divertor is therefore a natural sink for the plasma and charged particles reaching the walls will most likely recombine and be re-released as neutrals ("recycling") [4]. The occurring high neutral densities are beneficial to the pumping efficiency and as a result, the SOL in the main chamber of the plasma vessel remains at low impurity-densities.

Being the intentional point of plasma-wall contact, the Divertor is subjected to extreme heat and particle fluxes. The main problem is erosion and therefore release of impurities into the plasma, as well as material damage. At ASDEX Upgrade, the Divertor is made of tungsten, because it has a high melting point. On the other hand, tungsten is also an element of high atomic number(Z) and contamination of the plasma center, causes high energy losses by recombination-radiation. In order

to minimize the the Divertor load, special design considerations, to create a larger plasma-wetted area and thus flat angles of particle incidence, are taken into account. Also, neutral particle seeding (for example N_2) close to the Divertor, has shown to be efficient in inducing greater recombination radiation and scattering and thus decreasing temperature and net momentum flux onto the Divertor.

So, even though the plasma in a fusion device is in an ionized state and therefore mainly contained by the magnetic field, neutral particles are always present in the vessel, either from recycling processes or injected as fuel, although, of course, at very low densities. Understanding and controlling these densities in a fusion device is essential for successful operation. It is necessary to gain knowledge about the vacuum environment in the vessel and to be able to make predictions about the behavior of the neutral particle distribution, taking into account the real geometry. This understanding can also be helpful in designing a Divertor geometry, which allows efficient pumping of the vessel close to the Divertor.

1.4 Motivation of this Thesis

For small vessels and low vacuum densities, flows and distributions can be calculated on the basis of free-molecular flow, where nonlinear effects, such as collisions between particles, have no influence and the flow is entirely determined by the geometry and particle wall interactions. However, for higher densities or larger fusion devices, like ITER, vacuum conditions in the Divertor region shift towards a more fluid-like regime, the so called the transition regime, where collisions can no longer be neglected and nonlinear effects become relevant.

In principle, transition regime flows can be calculated numerically or analytically by kinetic theory, but for complex geometries like a vacuum vessel of a fusion device and the additional complexity brought about by the recombination and ionization of particles in the Divertor, calculating and predicting the behavior of neutral particle flows becomes virtually impossible by conventional methods. For these reasons computer-simulations are applied for the calculation of neutral particle distributions, for example Direct Simulation Monte Carlo (DSMC) or the Monte-Carlo code EIRENE developed by D.Reiter. *et al.* [5] (see Fig. 1.5). Because DSMC is usually a very computationally expensive method, calculations of conductances can take months, even with modern day computer power. Finding a reliable and efficient tool to calculate conductances for complex 3 dimensional structures is therefore highly desirable. EIRENE is a Monte Carlo code that relies on the BGK approximation of the Boltzmann equation and is therefore in principle suited to perform very efficiently, even for nonlinear problems.

So far the nonlinear scheme of EIRENE has only, although successfully, been tested on 2D Couette-flow. In this thesis EIRENE was benchmarked against well documented 3D-cases. A comparison has been made between vacuum conductances

calculated by EIRENE and results obtained from experiments and DSMC in the literature [6], [7], [8], [9] for validation and the agreement was found to be good.

At this point EIRENE is running based on the BGK approximation of the Boltzmann equation, which is known to be a good approximation for particle distributions but rather weak in determining temperature distributions [10]. For this thesis an extension of the code has been made to allow a more accurate calculation of temperature profiles. The extension was validated against the current version and the temperature profiles showed to be more realistic.

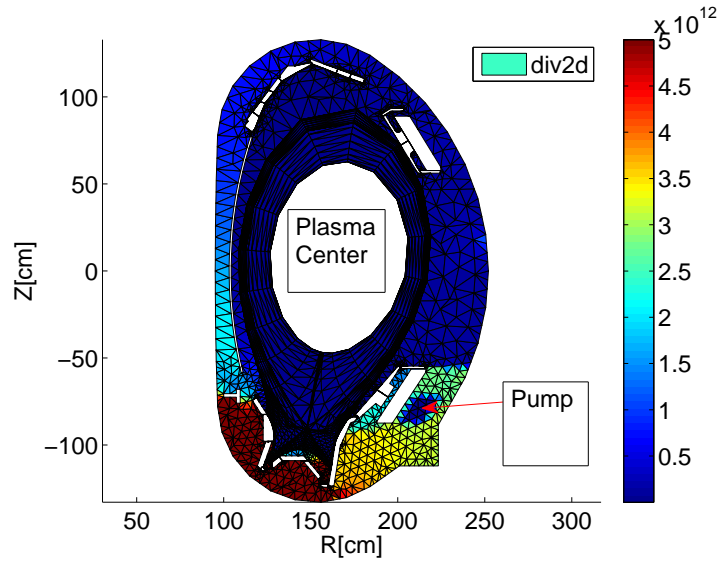


Figure 1.5: An example density distribution of neutral D_2 at ASDEX Upgrade, calculated by EIRENE

Chapter 2

Basic Concepts in Vacuum Physics

Vacuum physics is (usually) an applied science, at the boundary between fundamental statistical physics on the one side and vacuum engineering on the other. Since specific and at times differing experimental and theoretical definitions are found in the literature, it is important to state the basic concepts, this thesis relies on, for consistency reasons.

2.1 Conductance

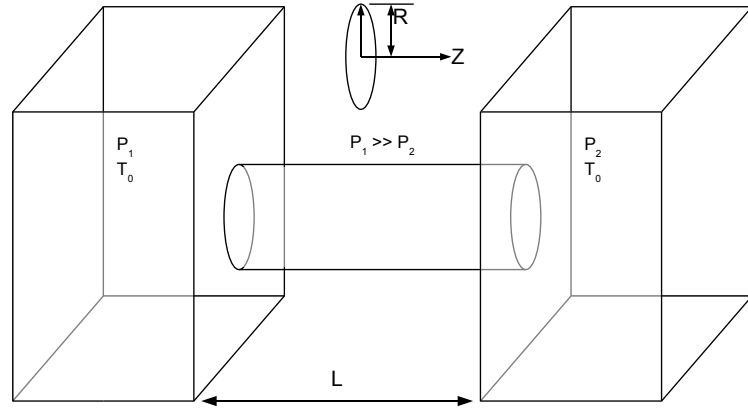


Figure 2.1: Two volumes with pressure P_1 and P_2 , connected by tube of length L

To become familiar with the conventions regarding rarefied gas flows, a few basic concepts need to be introduced first. In Fig 2.1 a schematic depiction is given of two semi-finite, connected volumes, where far from the inlet and the outlet, equilibrium conditions at different pressures $P_1 = n_1 k_B T$, $P_2 = n_2 k_B T$ and the same temperature T_0 are maintained to create a density-gradient driven flow. The conductance C is calculated as the particle flux $(\frac{\partial N}{\partial t})$ between the volumes over the particle-density

difference between the two volumes, as stated by Eq. 2.1 [11]

$$C = \frac{\frac{\partial N}{\partial t}}{n_1 - n_2} \quad (2.1)$$

or by the volumetric flow rate, over the pressure difference

$$C = \frac{\dot{Q}}{P_1 - P_2} \quad (2.2)$$

where \dot{Q} is the volumetric flow rate due to a pump with pumping speed S [11]:

$$\dot{Q} = P \frac{dV}{dt} = PS \quad (2.3)$$

2.2 Knudsen Number

The other fundamental concept is that of the Knudsen-number. It has the meaning of the ratio between the mean free-path λ over the typical dimension D of the conducting structure [12] and is a measure of the influence of boundaries for the development of the flow.

$$\text{Kn} = \frac{\lambda}{D} \quad (2.4)$$

For low densities, and therefore longer mean free path or small typical dimensions D , the Knudsen number will become large and the influence on the flow by particle-wall interactions will be greater than the influence by particle-particle interactions and vice versa. The mean free path λ , although being a microscopic quantity that can not be directly measured, can be expressed via a macroscopic quantity such as the viscosity μ . Because there is somewhat of a disagreement between definitions of the Knudsen number from different sources ([13] vs. [6] vs. [8]), for consistency in this thesis the Knudsen-number Kn will be defined as:

$$\text{Kn} = \frac{\sqrt{\pi}}{2} \frac{v_0 \mu}{k_B T_0 n_1} / D = \frac{\sqrt{\pi}}{2} \delta^{-1} \quad (2.5)$$

with the rarefaction parameter δ and $v_0 = \sqrt{\frac{k_B T}{2m}}$, the most probable velocity, following the convention of [13]. The viscosity is calculated to be $\mu = 1.7881 \cdot 10^{-7} \cdot (T[K])^{0.75}$ for D_2 self collisions [14]. The dimension D was taken as the radius R for circular apertures [15] and as the minor side-length(or height) h for rectangular apertures [16].

2.3 Flow-Regimes

The description of laminar flows, can generally be dealt with by hydrodynamic equations like the Navier-Stokes equations or Euler equations [17]. These are only valid as long as the continuum hypothesis holds, which means that the effects of interactions between the constituents are short-range compared to the characteristic dimension D of the system [17], like it is the case in a fluid, where collisionality is high and therefore the mean-free path is short $\lambda \ll D$ or $\text{Kn} < 0.1$. This case is called the "continuum" or "fluid regime".

For cases with low or zero collisionality, like high vacuum systems, the mean-free path well-exceeds the size of the characteristic dimension $\lambda \gg D$ or $\text{Kn} > 10$ and particle interactions can be neglected. The assumption of a continuum becomes invalid and flows can only be described by statistical equations originating from kinetic theory [18]. For negligible particle-particle interactions, the collision term in the Boltzmann Equation (Eq. 3.1) can be assumed to equal zero, rendering the kinetic equation linear and therefore analytical or numerical solutions more manageable. This case is also called the "Knudsen regime" or "free-molecular regime".

For cases where $0.1 \ll \text{Kn} \ll 10$, collisions can not be neglected and the continuum hypothesis is invalid as well [18]. In this so-called "transition regime", description of flows in general is difficult, except for highly idealized cases or with massive numerical effort. They are therefore usually treated by computer simulations like DSMC (Direct Simulation Monte Carlo) or EIRENE [19], [20].

Fig. 2.2 gives an overview of the flow regimes and corresponding current methods used to calculate solutions.

Range of Kn	Flow Regime	Governing equations	Numerical approach
$\text{Kn} \rightarrow 0$ $\delta \rightarrow \infty$	Continuum (inviscid)	Euler	Typical Computational Fluid Dynamic (CFD) schemes
$\text{Kn} < 10^{-1}$	Continuum (viscous)	Navier Stokes	
$10^{-1} \leq \text{Kn} \leq 10$	Transition	Boltzmann (BE) Kinetic models	Analytical methods (1D) Variational methods discrete velocity methods Integro-moment method DSMC
$10 < \text{Kn}$ ($\delta \rightarrow 0$)	Free molecular	BE and kinetic models <u>without</u> collisions	Method of characteristics Test Particle Monte Carlo

Figure 2.2: Overview of flow regimes and methods of solution

2.4 Calculation of conductance in the free-molecular or Knudsen regime and the concept of transmission probability

For collision-less flows into vacuum, the conductance through an aperture will be merely determined by the flux of the particles hitting the area A of the aperture so it can be simply calculated as

$$C_{FM_0} = \frac{A}{4} \cdot \sqrt{\frac{8kT}{\pi m}} = \frac{A}{4} \cdot \bar{v}_0 \quad (2.6)$$

where \bar{v}_0 is the mean speed [11]. For finite length ducts, a transmission probability can be calculated via the Clausing equation, a rather lengthy probabilistic integral equation, that will not be discussed here in detail [21]. The transmission probability, also called the Clausing-factor, gives the probability that a particle which has entered the aperture, would leave the duct and never return:

$$W = \frac{C}{C_{FM_0}} \quad (2.7)$$

In order to create a scale-free measure for conductance, for comparisons, any calculated or measured conductance can be normalized by C_{FM_0} , defining a normalized conductance W (also known as the "reduced flow rate") relative to the free molecular flux through the aperture, in the same way. This convention is commonly used throughout the vacuum community and will therefore be also applied in this thesis for all flow regimes.

In the free molecular flow regime, the first equation describing the conductance for long ducts was deduced by Knudsen from experimental and theoretical considerations:

$$C_{Knudsen} = \frac{4}{3} \bar{v}_0 \left[\int \frac{B}{A^2} dl \right]^{-1} \quad (2.8)$$

where B is the perimeter. For ducts of finite length or arbitrary cross-section, Eq. 2.8 was commonly used in context of the Knudsen-Dushman relation, which related the "resistance" (inverse conductance) of the orifice and the pipe to electrical resistors and is an electrical circuit analogy, for a handy approximation:

$$\frac{1}{C_{effective}} = \frac{1}{C_{FM_0}} + \frac{1}{C_{Knudsen}} \quad (2.9)$$

This formula was widely used throughout the 20th century to calculate conductances of free-molecular flows, although it's theoretical flaws were pointed out early

by Smoluchowski in 1910 [22]. Smoluchowski's corrections lead to a formula for infinitely long ducts of arbitrary cross-section

$$C_{Smoluchowski} = \frac{\bar{v}_0}{8l} \int_s \int_{-\pi/2}^{+\pi/2} \frac{1}{2} \rho^2 \cos \theta d\theta ds \quad (2.10)$$

where ρ is a chord making an angle θ with the normal of the perimeter s .

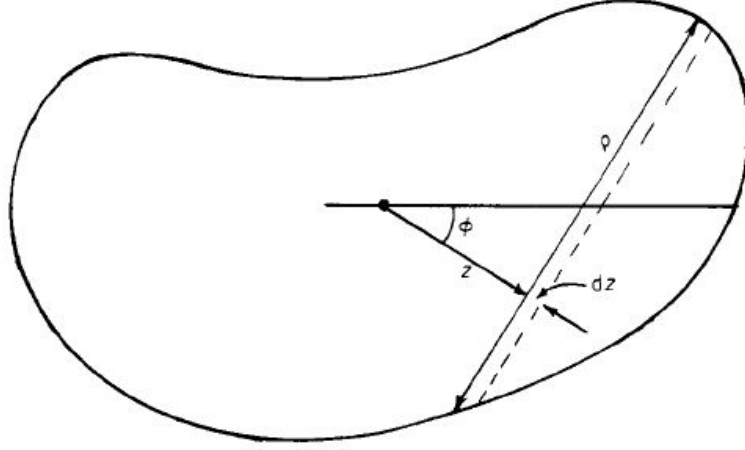


Figure 2.3: Cross-section of general shape. The chord, length ρ , is shown at the angle $(90^\circ - \theta)$ to a fixed line [23] and s for the calculation of Eq. 2.10

Indeed, Steckelmacher unveiled the discrepancies between those two approaches in 1978 [24], showing that for long rectangular ducts with high aspect ratios the Knudsen-formula underestimated the real conductance up to 56%.

Clausing, also disagreeing with the assumptions made by the Knudsen-Dushman formula, had presented a probabilistic integral equation as early as 1932 for finite-length ducts of circular and rectangular cross-sections [21] that can be solved numerically.

The Clausing equation is still valid today and the resulting Clausing-factors have been recalculated to a higher accuracy and extended to include more radius-to-length ratios by Cole (found in [11] in tabulated form) and Berman (Eq. 2.11) found in [11]) for finite-length circular tubes and by Santeler and Boeckmann, Cole (all found in [11] in tabulated form for different side-length- and length-ratios) and Berman (Eq. 2.12 found in [11]) for finite length rectangular ducts. Berman presented an equation for the transmission probability (Eq. 2.7) for finite length circular ducts of radius R and length l :

$$W = 1 + y^2 - y\sqrt{y^2 + 1} - \frac{\left[(2 - y^2) \sqrt{y^2 + 1} + y^3 - 2 \right]}{4.5y\sqrt{y^2 + 1} - 4.5\ln \left[y + \sqrt{y^2 + 1} \right]}, \text{ with } y = \frac{l}{2R} \quad (2.11)$$

which agrees to the data of Cole within 0.13%. For rectangular ducts, Berman derived another formula for short, narrow and rectangular ducts ($b \gg a$ and $b \gg l$, with a, b the sidelength and l the length)

$$W = 0.5 \left[1 + \sqrt{1 + x^2} - x \right] - \frac{1.5 \left[x - \ln(x + \sqrt{1 + x^2}) \right]^2}{x^3 + 3x^2 + 4 - (x^2 + 4)\sqrt{1 + x^2}} \quad (2.12)$$

Both formulas were found in [11]. There exists a number of tabulated data for specific types of shapes and geometries, all calculated numerically or by Monte Carlo methods.

2.5 Calculation of conductance in the transition-flow-regime

Investigation of flows in the transition regime is still an active field of research as the great number of recent publications might prove [25], [9], [26], [27], [28], [29], [30]. There are several codes and empirical data dealing with this issue and for the validation performed in this thesis four articles stood out.

For short tubes and orifices it was the work performed by Tetsuo Fujimoto and Masaru Usami, who provided experimental data over a wide range of problems [6]. As their definition of the Knudsen number differs from the definition used in this thesis (Eq. 2.5) and their empirical formula is given in terms of the Reynolds number, let's first consider the transformation from Knudsen number to Reynolds number:

The Reynolds number Re in [6] is defined as

$$Re = 0.501 \text{Kn}_{FU}^{-1} * W \approx \text{Kn}^{-1} * W \quad (2.13)$$

Note that the definition for the Knudsen number given in [6] varies from the definition given in Eq. 2.5, because it considers the diameter as the dominating dimension, not the radius ($\text{Kn}_{FU} = \frac{1}{2}\text{Kn}$). The formula given for short tubes in the transition regime, valid in the range of $Re < 2800$ (or $\text{Kn} > 5 \cdot 10^{-4}$ for circular orifices) for low pressure ratios ($\frac{P_2}{P_1} < 0.01$) is stated as:

$$W = \frac{0.4733 + I\sqrt{1/(aRe)^c}}{1 + J/(aRe)^c + K/(aRe)^{2c}} b + \frac{C_{FM}}{C_{FM_0}} \quad (2.14)$$

with $I = 1.31(C_{FM}/C_{FM_0})^{16}$, $J = 8.537$, $K = 3.599$ and a, b, c being parameters depending on the length to radius ratio $\frac{R}{l}$, tabulated for specific values (see appendix: 7.1). As a value for $\frac{C_{FM}}{C_{FM_0}}$ the Berman-approximation (Eq. 2.11) was used. Please not that Eq. 2.14 is a nonlinear implicit function. It was solved numerically by a root-finding algorithm, solving $0 = W - W(W)$, for the range of W in question.

For flows through rectangular orifices at low pressure ratios ($\frac{P_2}{P_1} < 0.01$) an publication by F.Sharipov and D.Kozak [7] provided a formula for flow into vacuum ($\frac{P_2}{P_1} = 0$), derived from a DSMC solution with less then 0.5% numerical uncertainty.

$$W = 1 + \frac{0.1736 \left(\frac{\pi}{2Kn}\right) + 0.0035 \left(\frac{\pi}{2Kn}\right)^2}{1 + 0.2754 \left(\frac{\pi}{2Kn}\right) + 0.006477 \left(\frac{\pi}{2Kn}\right)^2} \quad (2.15)$$

For flows at finite pressure ratio $0 < \frac{P_2}{P_1} < 1$ an semi-empirical formula has been derived by A.K. Sreekanth [8] for tubes of finite length. With the convention for the Knudsen number and normalized conductance in this thesis the equation is stated as

$$W = \frac{1}{1 + L/(2R)} \left[\frac{1 + P_2/P_1}{10Kn} + 1.038 \right] \quad (2.16)$$

Also in the article [9], the values for $W(1 - \frac{P_2}{P_1})$ were given in tabulated form for finite pressure differences, $\frac{P_2}{P_1} = 0.1, 0.5, 0.7$ at rarefaction numbers between 0.1 and 1000.

2.6 Calculation of conductance in the continuum-flow-regime

For viscous laminar flows, where the Mach-number is small ($Ma < 0.3$), the Hagen-Poiseuille equation is stated as [11]:

$$\dot{Q} = \frac{\pi R^4 |\Delta P|}{8\mu l} \bar{P} \quad (2.17)$$

When used with the definition of conductance in Eq. 2.2, it leads to an equation for conductance for long circular pipes [11]:

$$C = \frac{\pi R^4}{8\mu l} \bar{P} \quad (2.18)$$

where $\bar{P} = \frac{P_1 + P_2}{2}$ is the average pressure over both volumes. A similar equation can be approximated for rectangular ducts [11]

$$C = \frac{1}{12\mu l} \frac{a^3 b^3}{(a^2 + b^2 + 0.371ab)} \bar{P} \quad (2.19)$$

which corresponds to the solution of the Navier-Stokes equation for laminar flows [25].

The maximum conductance in the continuum flow regime is stated by the Euler limit, where for a critical value of the pressure ratio [31]

$$P_2/P_1 = [2/(\gamma + 1)]^{\gamma/(\gamma-1)} \quad (2.20)$$

with γ the adiabatic coefficient, the conductance can be described by

$$\frac{C}{C_{FM_0}} = W = \gamma^{1/2} \left(\frac{2}{\gamma + 1} \right)^{(\gamma+1)/[2(\gamma-1)]} \sqrt{2\pi} * A(\gamma) \quad (2.21)$$

with $A(\gamma) = 1$ for an ideal nozzle [32] and $A(\gamma) = 0.85$ for flow of a mono-atomic gas ($\gamma = 5/3$) through an aperture [11]. It gives a maximum normalized conductance of $W_{max} = 1.53$ for an aperture and $W_{max} = 1.82$ for an ideal nozzle and serves as an asymptotic limit for all tubes and orifices, as long as the flow remains laminar.

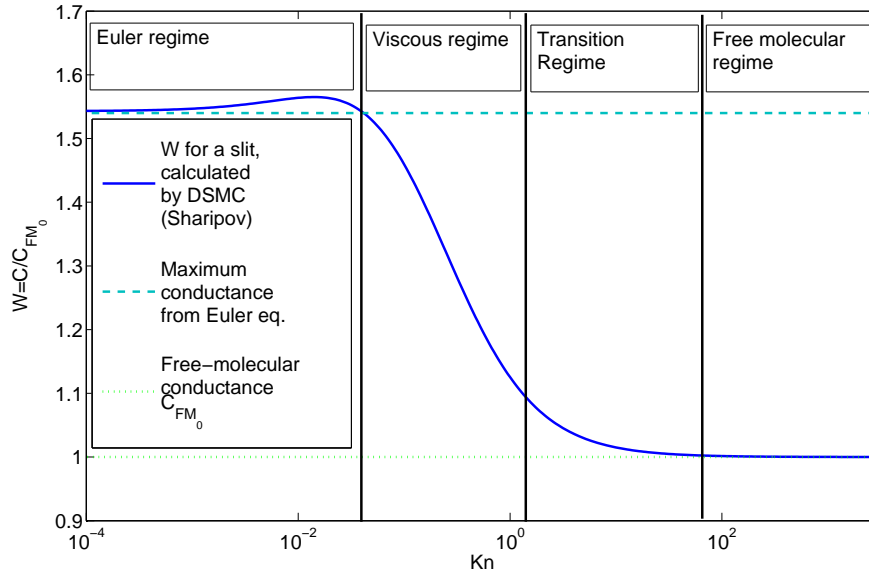


Figure 2.4: $W = \frac{C}{C_{FM_0}}$, the ratio between the actual conductance and the free molecular conductance of the aperture. The figure displays an example for a slit. Different Regimes are labeled. The Free-molecular W and the Euler limit W are indicated by dotted lines.

Chapter 3

Kinetic Equations and Monte Carlo Simulations

In the following chapter an overview is presented over the most basic properties of the Boltzmann equation and the Monte-Carlo approach of solution. It includes an introduction to the BGK approximation, which is deployed in EIRENE, as well as the elliptical BGK approximation that was implemented as an extension of the code as part of this thesis.

3.1 The single species Boltzmann Equation

Originally developed to describe transport processes in rarefied gas, the Boltzmann equation became one of the most fundamental equations in non-equilibrium statistical mechanics and is now applied in a broad range of fields, from quantum mechanics over solid state physics to galactic dynamics. It is based on the "*Stosszahlansatz*", taking into account only two-body collisions of particles that are uncorrelated prior to the collision [33]. A common form is written as:

$$\left[\frac{\partial}{\partial t} + \mathbf{v} \cdot \nabla_{\mathbf{r}} + \frac{\mathbf{F}(\mathbf{r}, \mathbf{v}, t)}{m} \cdot \nabla_{\mathbf{v}} \right] f(\mathbf{r}, \mathbf{v}, t) = \int \int \int \sigma(\mathbf{v}', \mathbf{V}', \mathbf{v}, \mathbf{V}) |\mathbf{v}' - \mathbf{V}'| f(\mathbf{v}') f_b(\mathbf{V}') d\mathbf{v}' d\mathbf{V} d\mathbf{V}' \\ - \int \int \int \sigma(\mathbf{v}, \mathbf{V}, \mathbf{v}', \mathbf{V}') |\mathbf{v} - \mathbf{V}| f(\mathbf{v}) f_b(\mathbf{V}) d\mathbf{v}' d\mathbf{V} d\mathbf{V}' \\ + Q(\mathbf{r}, \mathbf{v}, t) \quad (3.1)$$

with $f(\mathbf{r}, \mathbf{v}, t)$ or $f(x)$ being the *one particle distribution function* for a state x in 6N-phase-space characterized by a position vector \mathbf{r} and a velocity vector \mathbf{v} and f_b being the corresponding distribution function for the collision partner, from now on called "background distribution" (which for single species is of course $f_b = f$). \mathbf{v}' and \mathbf{V}' are the velocities prior to collision and $\sigma(\mathbf{v}, \mathbf{V}, \mathbf{v}', \mathbf{V}')$ is the impact parameter acting on the particle.

Furthermore $\mathbf{F}(\mathbf{r}, \mathbf{v}, t)$ is the volume force field, m is the particle mass and $Q(r, v, t)$ is a source-term. The left-hand side of the equation corresponds to the description of free-flight, while the right-hand side is the Boltzmann-collision integral $(= (\frac{\partial f}{\partial t})_{coll})$, describing the evolution of the system due to collisions (gain and loss from velocity space interval $[\mathbf{v}, \mathbf{v} + d\mathbf{v}]$), boundary conditions as well as any sources [5].

Although the equation is algebraically very complex it has a simple physical content: conservation in phase space. All macroscopic quantities, that is particle density $n(t, \mathbf{r})$, drift velocity $\mathbf{u}(t, \mathbf{r})$, pressure $P(t, \mathbf{r})$, the pressure tensor $P_{ij}(t, \mathbf{r})$ and the temperature $T(t, \mathbf{r})$ can be calculated as moments of $f(\mathbf{r}, \mathbf{v}, t)$ [34].

$$n(t, \mathbf{r}) = \int f(t, \mathbf{r}, \mathbf{v}) d\mathbf{v} \quad (3.2)$$

$$\mathbf{u}(t, \mathbf{r}) = \frac{1}{n(t, \mathbf{r})} \int \mathbf{v} f(t, \mathbf{r}, \mathbf{v}) d\mathbf{v} \quad (3.3)$$

$$P(t, \mathbf{r}) = \frac{m}{3} \int (\mathbf{v} - \mathbf{u})^2 f(t, \mathbf{r}, \mathbf{v}) d\mathbf{v} \quad (3.4)$$

$$P_{ij}(t, \mathbf{r}) = m \int (v_i - u_i)(v_j - u_j) f(t, \mathbf{r}, \mathbf{v}) d\mathbf{v} \quad (3.5)$$

$$T(t, \mathbf{r}) = \frac{m}{3n(t, \mathbf{r})k_B} \int (\mathbf{v} - \mathbf{u})^2 f(t, \mathbf{r}, \mathbf{v}) d\mathbf{v} \quad (3.6)$$

where k_B is the Boltzmann constant and m is the atomic mass.

For neutral particle transport there are no external forces acting on the particle (except for momentum exchange in collisions) so the equation simplifies further ($\mathbf{F} = 0$) and we end up with a more readable notation [35]:

$$\frac{\partial f(\mathbf{r}, \mathbf{v}, t)}{\partial t} + \mathbf{v} \cdot \vec{\nabla}_r f(\mathbf{r}, \mathbf{v}, t) = (\frac{\partial f}{\partial t})_{coll} \quad (3.7)$$

The following important properties are highlighted[35]:

1. Equilibrium: In states of thermodynamic local equilibrium $\frac{\partial f(\mathbf{r}, \mathbf{v}, t)}{\partial t} = 0$ and $\mathbf{v} \cdot \vec{\nabla}_r f(\mathbf{r}, \mathbf{v}, t) = 0$, and therefore the collision integral vanishes as well $(\frac{\partial f}{\partial t})_{coll} = 0$. In this case the solution of Eq. 3.1 $f(\mathbf{r}, \mathbf{v}, t)$ is a Maxwellian distribution f_M .

2. H-Theorem: If for any distribution function $f(\mathbf{r}, \mathbf{v}, t)$

$$H(f(\mathbf{r}, \mathbf{v}, t)) = \int_{R^3} f(\mathbf{r}, \mathbf{v}, t) \ln f(\mathbf{r}, \mathbf{v}, t) d\mathbf{v} \quad (3.8)$$

is defined, for any $f(\mathbf{r}, \mathbf{v}, t)$ that evolves according to the Boltzmann equation, the function

$$\mathcal{H} = \int_D H(f(\mathbf{r}, \mathbf{v}, t)) d\mathbf{r} \quad (3.9)$$

with $\delta D \in R^3$ a nonporous, nonconducting wall around a homogeneous region D , the relation

$$\frac{d\mathcal{H}}{dt} \leq 0 \quad (3.10)$$

holds. So the Boltzmann equation describes a "relaxation" towards a state of minimum \mathcal{H} , the final state being a steady state and thus a Maxwellian f_M having the maximum entropy.

3. Euler Equations: For $f(\mathbf{r}, \mathbf{v}, t) = f_M(\mathbf{r}, \mathbf{v}, t)$, a local Maxwellian, the moments derived by Eq. 3.2-3.6 $n(t, \mathbf{r})$, $\mathbf{u}(t, \mathbf{r})$, $P(t, \mathbf{r})$ and $T(t, \mathbf{r})$ satisfy the Euler equations of motion:

$$m \frac{\partial n(t, \mathbf{r})}{\partial t} = m \vec{\nabla} \cdot (n(t, \mathbf{r}) \mathbf{u}(t, \mathbf{r})) = 0 \quad (3.11)$$

$$m \frac{\partial (n(t, \mathbf{r}) \mathbf{u}(t, \mathbf{r}))}{\partial t} + m \vec{\nabla} \cdot (n(t, \mathbf{r}) \mathbf{u}(t, \mathbf{r}) \otimes \mathbf{u}(t, \mathbf{r})) + \vec{\nabla} \cdot P(t, \mathbf{r}) = 0 \quad (3.12)$$

$$m \frac{\partial (n(t, \mathbf{r}) E(t, \mathbf{r}))}{\partial t} + \vec{\nabla} \cdot (\mathbf{u}(t, \mathbf{r}) (mn(t, \mathbf{r}) E(t, \mathbf{r}) - P(t, \mathbf{r}))) = 0 \quad (3.13)$$

while for the last equation the total energy $E(t, \mathbf{r}) = \frac{1}{2} mn(t, \mathbf{r}) |\mathbf{u}(t, \mathbf{r})|^2 + \frac{3}{2} n(t, \mathbf{r}) k_B T(t, \mathbf{r})$ was used for convenience.

3.2 Treatment of the Boltzmann Collision Integral

For linear transport problems "the background" distribution $f_b(\mathbf{V})$ is given, so the function $f(\mathbf{v})$ can be taken out of the second integral in Eq. 3.1, to arrive at the following equation [14]:

$$\begin{aligned} \frac{\partial f(\mathbf{r}, \mathbf{v}, t)}{\partial t} + \mathbf{v} \cdot \nabla_{\mathbf{r}} f(\mathbf{r}, \mathbf{v}, t) + \nu_t(\mathbf{r}, \mathbf{v}) f(\mathbf{r}, \mathbf{v}, t) = \int d\mathbf{v}' C(\mathbf{r}; \mathbf{v}' \rightarrow \mathbf{v}) |\mathbf{v}' - \mathbf{V}'| f(\mathbf{r}, \mathbf{v}, t) \\ + Q(\mathbf{r}, \mathbf{v}, t) \end{aligned} \quad (3.14)$$

Here $\nu_t(\mathbf{r}, \mathbf{v})$ is the total collision frequency and $C(\mathbf{r}, \mathbf{v}' \rightarrow \mathbf{v})$ is the kernel of the collision operator.

The collision frequency is the sum over all collision frequencies ν_k from every collision process k and also includes surface collisions [14]:

$$\begin{aligned}\nu_t(\mathbf{r}, \mathbf{v}) &= \sum_k \nu_k(\mathbf{r}, \mathbf{v}) \\ \nu_k(\mathbf{r}, \mathbf{v}) &= \int \int \int \sigma_k(\mathbf{v}, \mathbf{V}, \mathbf{v}', \mathbf{V}') |\mathbf{v} - \mathbf{V}| f_b(\mathbf{V}) d\mathbf{v} d\mathbf{V} d\mathbf{V}'\end{aligned}\quad (3.15)$$

The collision kernel gives the number of particles with velocity (\mathbf{v}') which emerge from collision processes k (particle-particle as well as particle-surface collisions) with velocity (\mathbf{v}) [14]:

$$\begin{aligned}C(\mathbf{r}; \mathbf{v}' \rightarrow \mathbf{v}) &= \sum_k \nu_k(\mathbf{r}, \mathbf{v}') c_k(\mathbf{r}, \mathbf{v}' \rightarrow \mathbf{v}) \\ c_k(\mathbf{r}; \mathbf{v}' \rightarrow \mathbf{v}) &= \frac{\int \int \sigma(\mathbf{v}', \mathbf{V}'; \mathbf{v}, \mathbf{V}) |\mathbf{v}' - \mathbf{V}'| f_b(\mathbf{V}') d\mathbf{V}' d\mathbf{V}}{\int \int \int \sigma(\mathbf{v}', \mathbf{V}', \mathbf{v}, \mathbf{V}) |\mathbf{v}' - \mathbf{V}'| f_b(\mathbf{V}) d\mathbf{v}' d\mathbf{V} d\mathbf{V}}\end{aligned}\quad (3.16)$$

The factor $c_k(\mathbf{r}; \mathbf{v}' \rightarrow \mathbf{v})$ is the conditional probability distribution for the post-collision velocity \mathbf{v} .

Generally the collision probability $c_k(\mathbf{r}', \mathbf{v}' \rightarrow \mathbf{v})$, should give a maximum of uncertainty about the velocity with which a particle will emerge from a collision. This can be achieved by maximizing the local Shannon-entropy S , known from information theory, using the (normalized) probability for the emergent velocity[36]

$$\psi(\mathbf{r}', \mathbf{v}) = 1/n(\mathbf{r}') \cdot \int c(\mathbf{r}', \mathbf{v}' \rightarrow \mathbf{v}) d\mathbf{v}' \quad (3.17)$$

$$S(\mathbf{r}) = - \int \psi(\mathbf{r}', \mathbf{v}) \ln \psi(\mathbf{r}', \mathbf{v}) d\mathbf{v} \quad (3.18)$$

To find the extremum (i.e. the equilibrium) of this equation, the variation ($\delta S = 0$) can be solved by Lagrangian multipliers, which will have to satisfy the conservation laws stated by Eq. 3.19 [36].

$$\int \left(\frac{\delta f}{\delta t} \right)_{coll} \Theta(\mathbf{v}) d\mathbf{v} = 0 \quad (3.19)$$

with $\Theta \mathbf{v} = 1, v_x, v_y, v_z, \mathbf{v}^2$, which is equivalent to the fluid motion conservation laws stated by the Euler equations Eq. 3.11-3.13.

Also, considering only stationary problems, explicit time dependence can be neglected and therefore the partial time derivative vanishes ($\frac{\partial f}{\partial t} = 0$).

3.3 The BGK approximation

In the free-molecular regime, particle-particle collisions can be neglected, rendering the collision integral in the Boltzmann equation linear, so the collision kernel $C(\mathbf{r}' \rightarrow \mathbf{r}, \mathbf{v}' \rightarrow \mathbf{v})$ will only depend on the boundaries and not on the distribution of any possible collision partners (f_b). However, in the transition regime ($\text{Kn} \leq 10$) particle-particle collisions can not be neglected, the collision integral becomes nonlinear in \mathbf{v} and therefore, in general hard to solve by conventional methods, except for highly idealized cases [19].

To linearize the collision integral for particle-particle collisions the Bhatnagar, Gross and Krook (BGK) collision model can be introduced, by assuming the collision integral $(\frac{\delta f}{\delta t})_{coll}$ to describe a relaxation of $f(x)$ toward the local equilibrium, a drifting Maxwellian distribution [19]

$$f_M = n \cdot \psi(\mathbf{v})_M = (2\pi n k_B T)^{-\frac{3}{2}} \exp(-[(\mathbf{v} - \mathbf{u})^2 / 2k_B T]) \quad (3.20)$$

within a relaxation time τ :

$$(\frac{\delta f}{\delta t})_{coll} \rightarrow (\frac{\delta f}{\delta t})_{BGK} = \frac{f(\mathbf{r}', \mathbf{v}') - f_M(\mathbf{r}', \mathbf{v}')}{\tau} \quad (3.21)$$

It can be shown [37] that the BGK model reproduces the equilibrium solution $f = f_M$ and the conservation of mass, momentum and energy at equilibrium (Eq. 3.19), resulting in the moment relations:

$$\int v_i \psi_M(\mathbf{v}) d\mathbf{v} = u_i \quad (3.22)$$

$$\int (v_i - u_i)(v_i - u_i) \psi_M(\mathbf{v}) d\mathbf{v} = 3n k_B T \quad (3.23)$$

The BGK approximation also holds the H-theorem and leads to the Navier-Stokes equations when the Chapman-Enskog expansion is applied [38]. The relaxation time (in the case of single species and elastic collisions, corresponding to the inverse total collision frequency $\frac{1}{\nu_t}$) τ can be obtained in terms of dynamic viscosity μ [10]:

$$\tau = \frac{\mu}{n k_B T} \quad (3.24)$$

Alternatively it can be obtained using the coefficient of thermal conductivity κ [10]:

$$\tau = \frac{2}{5} \frac{m}{k_B} \frac{\kappa}{n k_B T} \quad (3.25)$$

The Prandtl number is a dimensionless number defined as a ratio

$$\text{Pr} = \frac{\text{viscous diffusion rate}}{\text{thermal diffusion rate}} = \frac{c_p \mu}{\kappa} \quad (3.26)$$

where $c_p = \frac{5}{2}k_B T$ is the specific heat for monoatomic gases.

Here, the first disadvantage of the BGK model becomes apparent, since for both relaxation times to match, the Prandtl-number will become unity, whereas it usually differs appreciably from unity for most real gases ($\text{Pr} \approx \frac{2}{3}$). It should be noted that τ does not depend on the velocity but only on the local particle density and temperature. None the less it has been shown to produce quantitatively good results when applied to isothermal flows of rarefied gases.

3.4 The ellipsoidal BGK approximation for correct Prandtl number

In an attempt to improve the BGK-approximation, the so called ellipsoidal BGK approximation (from now on referred to as ESBGK) has been developed in [36].

$$\left(\frac{\delta f}{\delta t}\right)_{coll} \rightarrow \left(\frac{\delta f}{\delta t}\right)_{BGKES} = \frac{f(\mathbf{r}', \mathbf{v}') - n \cdot \psi_{BGKES}(\mathbf{r}', \mathbf{v}')}{\tau_{BGKES}} \quad (3.27)$$

The ESBGK model satisfies all conditions for a valid collision model, one of which, the H-theorem has been proven to hold only recently in [38], reviving interest in the model. As a main advantage of the model, it includes a free parameter that can be adjusted to obtain a correct Prandtl number.

The underlying idea of the ESBGK model is to include so-called "persistence of velocity"-effects by the additional information of the second-order moments into the moment relation Eq. 3.23 [36]:

$$P_{ij}(\mathbf{r}) = m \cdot n \cdot \int (v_i - u_i)(v_j - u_j) \psi(\mathbf{v}) d\mathbf{v} \quad (3.28)$$

Through maximizing the Shannon entropy and using Eq. 3.28 as an additional constraint, the emitted velocity probability distribution $\psi_{BGKES}(\mathbf{v})$ results in an anisotropic Gaussian:

$$\psi_{BGKES}(\mathbf{v}) = (2\pi)^{-\frac{3}{2}} |\lambda|^{-\frac{1}{2}} \exp\left(-\frac{1}{2}(v_i - u_i) \epsilon_{ij} (v_j - u_j)\right) \quad (3.29)$$

where $|\lambda|$ is the determinant of λ , the tensor corresponding to λ_{ij} and ϵ_{ij} are the components of $\epsilon = \lambda^{-1}$, the tensor inverse to λ_{ij} [36]. Choosing λ_{ij} to be a linear function of the elements of the pressure tensor normalized by mass-density

$$m \cdot n \cdot \lambda_{ij} = G_{ijkl} P_{ij} \quad (3.30)$$

and considering that G_{ijkl} must be a symmetric, isotropic tensor, it follows that

$$m \cdot n \cdot \lambda_{ij} = (1 - b) P \delta_{ij} + b \cdot P_{ij} \quad (3.31)$$

including the free parameter b [36]. By applying the Chapman-Enskog expansion a relationship for the free parameter b can be stated depending on the Prandtl number [36]

$$b = (\text{Pr} - 1)/\text{Pr} \quad (3.32)$$

and the collision frequency depending on the viscosity

$$\nu_{ESBGK} = \frac{nk_B T}{\mu(1 - b)} \quad (3.33)$$

For $b = 0$, $\psi_{ESBGK}(\mathbf{v})$ is transformed into $\psi_M(\mathbf{v})$, yet again stating the ordinary BGK-model. For $b = -\frac{1}{2}$, the resulting Prandtl number will be such as to match the experimentally found Prandtl number of $2/3$ and the collision frequency will decrease [36].

3.5 Implemented Transformation

In the original sampling method for the BGK-model, implemented in EIRENE, the pre-collision velocities of the collision partners were sampled from a drifting 3D-Maxwellian-distribution. For the implementation of the ESBGK-model, the sampling distribution had to be transformed into the new distribution function denoted by Eq. 3.29. For a more readable notation, the peculiar velocity $\mathbf{c} = (\mathbf{v} - \mathbf{u})$ is introduced. The transformation

$$(v_i - u_i)\epsilon_{ij}(v_j - u_j) = c_i\epsilon_{ij}c_j = c^T\epsilon c = (A\zeta)^T\epsilon A\zeta = \zeta A^T\epsilon A\zeta = \sum_{k=1}^3 \zeta_k^2 \quad (3.34)$$

with $c = A\zeta$ and $A^T\epsilon A = \begin{pmatrix} 1 & 0 & 0 \\ 0 & 1 & 0 \\ 0 & 0 & 1 \end{pmatrix}$

will be used to allow collision sampling to still occur from a 3D-Maxwellian-distribution, while resulting velocities will be transformed back to obey the elliptic distribution function Eq. 3.29. To determine A , it is easily shown [10] that

$$A^T\epsilon A = \mathbb{I} \rightarrow A^T = A^{-1}\epsilon^{-1} \rightarrow A^T = A^{-1}\lambda \rightarrow A \cdot A^T = \lambda \quad (3.35)$$

Since λ is a symmetric matrix, there exists an equivalent notation in which A is a triangular matrix and therefore

$$\sum_{k=1}^{\min(i,j)} a_{ik}a_{jk} = \lambda_{ij} \quad (3.36)$$

becomes a simple set of fully determined linear equations, from which all entries a_{ij} can be derived. The emission probability for emergent particles reads:

$$\psi_{BGKES}(\mathbf{v}) = (2\pi)^{-\frac{3}{2}} |\lambda|^{-\frac{1}{2}} \exp\left(-\frac{1}{2} \sum_{k=1}^3 \zeta_k^2\right) \quad (3.37)$$

which is a 3D-Maxwellian. In order to obtain the new velocities, according to the distribution ψ_{BGKES} , the resulting samples ζ can be transformed back via $c_i = A_{ij} \zeta_j$.

3.6 EIRENE - BGK/BGKES

EIRENE is a neutral gas transport code, which calculates the distribution functions in 6-dimensional phase-space. In principle it is a multi-species code, solving simultaneously a system of time-dependent or stationary linear kinetic transport equations of almost arbitrary complexity.

Although the flexibility of EIRENE would allow for a wide range of possible applications, the work performed for this thesis focused on single species neutral gas flows and therefore the description will only be considered with this particular aspect of its application (further information can be received from the EIRENE manual on <http://www.eirene.de> [39]).

The Monte Carlo approach for solving Eq. 3.2 in EIRENE can be derived from its physical meaning [14]. Test particles will be generated, one at a time, according to the source distribution $Q(x)$, traveling along straight lines undergoing collisions with "background" particles and boundary surfaces at collision-frequencies ν_k , changing velocity according to the distribution $c_k(\mathbf{r}; \mathbf{v}' \rightarrow \mathbf{v}) d\mathbf{v}'$ until they reach an "absorbing state" x_a in the phase-space which, once reached, is never left again [5].

3.6.1 Sampling Free Path:

The mean free path l between two collisions can be sampled from the inverse cumulative distribution $F(l)$, since the collision ν_t is a parameter of EIRENE.

$$\begin{aligned} \text{for } l < l_{max} : \quad F(l) &= 1 - \exp \left[- \int_0^l \frac{\nu_t}{|\mathbf{v}|} ds \right] = 1 - u \\ \text{for } l \geq l_{max} : \quad F(l) &= \delta(l - l_{max}) \exp \left[- \int_0^{l_{max}} \frac{\nu_t(\mathbf{r})}{|\mathbf{v}|} ds \right] \end{aligned} \quad (3.38)$$

where l_{max} is the distance of the flight to the next boundary or internal surface where the test flight shall be stopped. u here is a random number distributed uniformly between 0 and 1. At the point of collision, u is sampled and $-\int_0^l \frac{\nu_t}{|\mathbf{v}|} ds$ is updated for each cell along the trajectory s until it meets the equality Eq. 3.38 [14].

3.6.2 Collision - Sampling

The collision probability $c_k(\mathbf{r}', \mathbf{v}' \rightarrow \mathbf{v})$ in this case is a distribution typical for elastic collisions or surface reflections. Several surface-reflection models are implemented in EIRENE, namely the Behrisch-Matrix model or TRIM code database reflection models [5].

For particle-particle collisions, thermalization with the "back-ground" is assumed and post collision velocities are sampled from the local equilibrium velocity distribution $\psi(x)$. For EIRENE-BGK this was the local drifting Maxwellian distribution Eq. 3.20 and for EIRENE-BGKES this was accomplished by transforming the samples from a Maxwellian distributions according to Eq. 3.34.

3.6.3 Successive Linearization Method

For EIRENE-BGK, an iterative procedure ("successive linearization") is applied, using the moments derived from a previous iteration to determine the local collision velocity distribution $\psi_M(= f_b/n)$ or $\psi_{BGKES}(= f_b/n)$ as a background of the new iterations. For each iteration the moments of $f(x)$ $\mathbf{u}(x)$, $T(x)$, $n(x)$ and $P_{ij}(x)$ are calculated, as well as all other derived quantities (for example: total energy, drift energy, etc). These moments are then again used to define new local Maxwellians ($\psi = f_b/n$). Iterations are repeated until the local equilibrium distribution $(\frac{\partial f}{\partial t})_{coll} = 0$, or equivalently stated $f_b = f$, is reached.

3.6.4 Responses

Detailed knowledge of the function $f(x)$ is not required, but only of a set of moments of this distribution. In order to do so, a discrete Markoff chain $\omega^n = (x_0, x_1, x_2, \dots x_n)$ is generated using $Q(x)$ as a initial distribution, $F(l)$ (Eq. 3.38) as a distribution of the free path and $\psi(\mathbf{v})$ (Eq. 3.20) as a distribution of the velocity \mathbf{v} [14].

To create such a chain, pseudo-random numbers (ξ_1, ξ_2, \dots) are generated according to the distributions Q , ψ and F . After the calculation of N (\approx several thousand) histories, the responses R are taken as the arithmetic mean of an estimator $X(\omega)$ [14].

$$R = \tilde{R} = \frac{1}{N} \sum_{i=1}^N X(\omega_i) \quad (3.39)$$

By increasing N the response R can be made arbitrarily precise. $X(\omega_i)$ depends on the type of estimator. For the collision estimator:

$$X_C(\omega_i) = \sum_{j=1}^n g_c(x_j) w(x_j) \quad (3.40)$$

Here g_c is the detector function which is calculated for each collision and $w(x_j)$ is the so called statistical weight. In the simplest case $g_c = 1$, this estimation yields the total number of collisions. It can be shown that X_C gives unbiased estimation of the sum of g_c over all collisions [14].

For the track-length estimator:

$$X_T(\omega_j) = \sum_{j=1}^n \int_{x_j}^{x_{j+1}} \frac{ds}{|v(s)|} g_t(s) w(s) \quad (3.41)$$

Here $g_t(s)$ is the detector function which is defined in each point of the particle's trajectory. This estimator gives the unbiased estimation of the corresponding moment of the distribution function:

$$\int f(\mathbf{r}, \mathbf{v}) g_t(\mathbf{r}, \mathbf{v}) d\mathbf{v} \quad (3.42)$$

It means that the sum over residence time of the particles in a volume is proportional to the number of particles in this volume. The estimators can be applied to any volume, in particular to each cell of the computational grid to get the spatially resolved estimation [14].

3.6.5 Statistical Error

One advantage of a Monte-Carlo method of calculation is that it inherently yields a result for the statistical error of the calculation. The variance per history is obtained as

$$\sigma_1^2(N) = \frac{1}{N-1} \sum_{i=1}^N (X_i - \bar{X})^2 \quad (3.43)$$

where $X_i = X(\omega_i)$ is the contribution of Monte Carlo history ω_i to estimator X for each moment of f (referred to as a "tally") and N is the number of Monte Carlo histories[14]. Due to the Central Limit theorem, the final estimate for the variance will be indirectly proportional to N

$$\sigma^2(N) = \frac{1}{N} \sigma_1^2(N) \quad (3.44)$$

so the standard deviation scales as $\sigma = 1/\sqrt{N}$ [14].

Chapter 4

Grid Generation and Methods of Evaluation

The EIRENE code is intended as a highly flexible tool to calculate particle distributions so therefore setting options are plentiful. In this chapter an overview of the most relevant settings is given, followed by a detailed description of the geometrical grids used for the validation. In the last part of this chapter possible sources of error are being discussed.

4.1 The EIRENE Input-file

EIRENE is configured by a formatted input-file (Sec. 7.2) that gives full control over the flexibility of the code. The input-file will include all settings for the operational mode, the geometrical (e.g. boundaries and sources) and physical properties (e.g. interactions and particles) as well as the output. The plentiful options can be looked up in the manual [5], so this description will focus on the options that were most relevant for this work.

4.1.1 Input Block 1: Input data for operating mode

This block controlled some of the more general options in EIRENE such as overall running time, number of iterations and usage of dump files. Also a few parameters depending on the simulation model (drifts included or not, etc.) [5].

4.1.2 Input Block 2: Input data for standard mesh

In this section, the boundaries of the mesh-cells are defined by co-ordinate surfaces, called "standard mesh surfaces". There are up to three sets of standard surfaces, corresponding to a radial- or x-dimension, a poloidal- or y-dimension and a toroidal- or z-dimension, depending on the geometry level. There are several geometry-level options: cartesian co-ordinates (x,y,z), a 2D "finite element" triangular mesh, and several others that will not be discussed here. For cartesian co-ordinates as well as for

the toroidal dimension, the number of surfaces as well as two zones of equidistant discretizations could be defined. For the triangular option, an external routine (TRIA by [Boerner, FZJ]) generated a 2 dimensional triangular mesh and co-ordinates of the triangles were loaded into the radial-dimension array, disabling the poloidal dimension array. The toroidal- or z-dimension could be set straight (grid in z-direction), or as an approximation by a number (≥ 30) of straight cylinders for both cartesian and triangular mesh options [5].

4.1.3 Input Block 3A: Non-default Standard Surfaces

In this input block surfaces from the standard mesh or subregions of the surfaces, could be set to non-default properties such as reflecting or absorbing. For triangular meshes, closed surface boundaries implemented in the mesh were recognized and could be set to non-default properties as well. Each non-default standard surface could be assigned a surface interaction model (defined in Input Block 6), an absorption coefficient or set to be specular reflective [5].

4.1.4 Input Block 3B: Additional surfaces

Additional surfaces could be configured by defining coefficients that were used as input parameters of an algebraic hyperbolic equation or inequality, to specify the boundary of the surface, i.e. the part of the surface which is seen by the test particles. The additional surfaces are independent of the co-ordinate system of the standard mesh and can be modeled individually in 3D cartesian co-ordinates. Each surface could also be assigned a surface interaction model (defined in Input Block 6), an absorption coefficient or set to be specular reflective analogously to the non-default standard surfaces [5].

4.1.5 Input Block 7: Input data for Initial Distribution of Test Particles

In this input block, the type of source distribution is set as either a point or a surface source and co-ordinates for position and direction are specified, as well as the temperature of the source. The flux could be supplied directly in units of [*Ampere*] or a density could be defined for a specific grid cell instead, as a scaling factor for all surface- or volume averaged results. Several different sources could be defined and CPU time is assigned to each, but by default CPU time was evenly split among each source. The seed for the random number generation is specified, either as a fixed seed (for repeatability) or as truly random (determined by machine clock). Also, the particle species emitted by the source is chosen [5].

4.2 General geometrical set-up

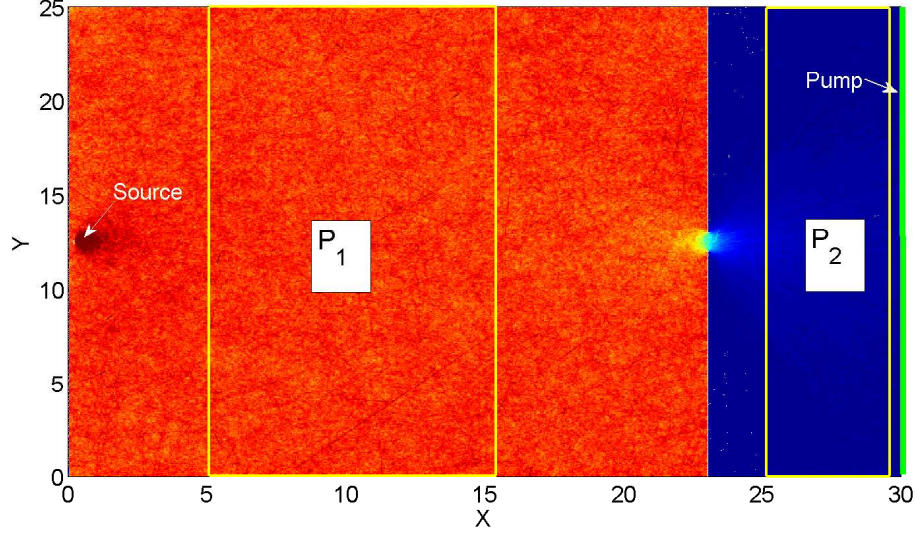


Figure 4.1: The figure displays a typical particle (density) distribution from a grid (slit) used for evaluating conductance. A source generates an evenly distributed particle density in a high pressure reservoir and an absorbing surface acts as a pump in a low pressure reservoir. Both reservoirs are connected by an conducting structure, causing a pressure gradient and therefore flow. The yellow marked areas represent pressure measurement areas where the pressure is evaluated as an average over each area.

In general the geometrical set-up consists of a high-pressure reservoir containing a neutral particle source that is connected to a low-pressure reservoir containing a pump (see Fig. 4.1). The ratio of the chamber dimensions to the typical dimension of the connection ought to be large to minimize influence on the conductance by the reservoir walls and to guarantee a uniform distribution. It should also be small enough to allow a sufficient throughput to generate particle histories by a reasonable computation time. The coarseness of the grid is restricted by available memory and CPU-time as well as the necessary resolution. The cell-size of the mesh determines the minimal Knudsen number that produces valid results, since it needs to be small enough to resolve any occurring gradients and allow the gas flow to develop correctly.

The source distribution is set as a point source emitting single-species thermal test-particles at $300K$ and the source-flux was set to establish certain Knudsen numbers. The boundary walls are assumed to be diffusively reflecting at a temperature of $300K$, being on the same temperature as the source. To calculate the conductance by Eq. 2.1, an average of the particle density is taken over a uniformly distributed part of the high-pressure reservoir as well as the low pressure reservoir (see Fig. 4.1).

The simulations were usually run to yield at least 1000 histories, to guarantee sufficiently low statistical error, and CPU time was set accordingly (300 – 5000s

per *iteration*). In non-linear mode, iterations were repeated until convergence was reached, although in general convergence was costly for low Knudsen numbers ($\text{Kn} < 0.1$; $\text{Nr.iteration} > 50$) (also see Sec. 4.6.1 for more detail).

The flow was aimed to be into vacuum, except when explicitly aiming for a flow with a finite pressure drop, so minimal pressure in the low pressure volume was desired. For the circular orifice the pressure ratio was around 0.1%, while for the slit, due to the larger opening, the pressure ratio could not be lowered further than to around 1.5% within the computational limits.

4.3 Grids with aperture of rectangular cross-section

Grids for modeling flows through apertures of rectangular cross-sections are generally more demanding in memory since large parts of the volume need to be finely meshed due to EIRENE being able to define only two zones of different sized discretizations per dimension. The comparatively large orifice area caused the pressure ratio ($\frac{P_2}{P_1}$) to be, in general, higher. But, on the other hand, allowed for more particle histories. The grids were usually produced having only one cell along the slit to exploit the symmetry and to save memory. Tests with more cells along the slit, to no surprise, showed no difference.

4.3.1 Grid for slit created by 2D-triangular mesh for free molecular length scan

The grid depicted in Fig. 4.2 and 4.3 was used to model the free-molecular flow through a rectangular duct, with length $0\text{cm} < l < 100\text{cm}$, height $h = 1\text{cm}$ and width $p = 10.366\text{m}$ (in z -direction). For the length scan, grids similar to this would be produced analogously for different l . A fine mesh ($\Delta t_1 = 1\text{cm}$) was applied in the area around the slit (Fig. 4.3), while the mesh in the remaining area was chosen to be coarser at ($\Delta t_2 = 10\text{cm}$). Since all runs performed on this grid were collisionless, cell-size was actually no constraint and CPU demands were very low at 1000s per Knudsen value (except for the 10m run, which was set to run for 50000s). The source was placed at the center of Y and Z at $x = 0.0001\text{cm}$ and the pump was set to be a 99% absorbing surface covering the whole opposing wall ($x = x_{\text{max}}$).

4.3.2 Grid for slit created by 2D-triangular mesh for Knudsen-scan

A similar grid, shown in Fig. 4.4 and 4.5, was used to model flow in the transition regime through a slit with height $h = 3\text{cm}$ ($= D$, the typical dimension defined in

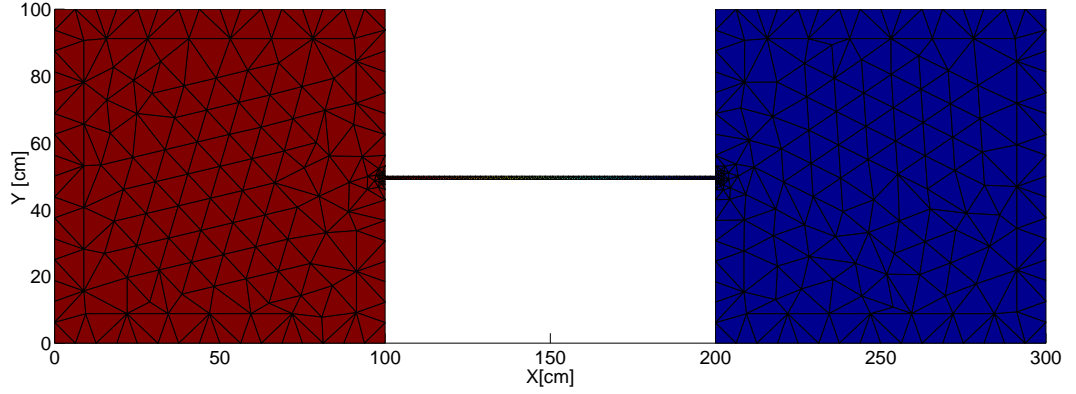


Figure 4.2: Grid for the free molecular length scan of a rectangular duct (height $h = 0.01m$ and depth $p = 10.37m$) generated by the TRIA routine. Two volumes of $1 \times 1 \times 10.37m^3$ are connected by a rectangular duct of finite length ($l = 100cm$ in this case). The source is placed in the left hand chamber, far away from the opening of the duct. The pump is modeled as an absorbing surface in the volume on the right hand side at $x = 300cm$.

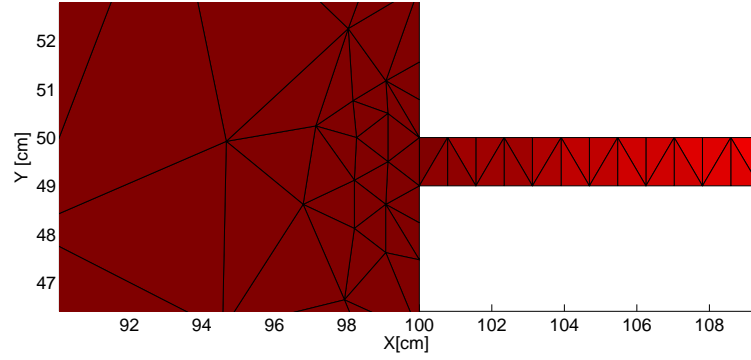


Figure 4.3: Close-up of the area surrounding a rectangular duct of height $h = 1cm$ (see Fig. 4.2, showing a fine discretization of the mesh: $\Delta t = 1.0cm$).

2.5) and width $p = 60cm$. The connected volumes were $60 \times 60 \times 60cm^3$. The meshing was produced to be finer ($\Delta t_1 = 0.03cm$) around the edges (giving a resolution of $\Delta t_1/D = 0.01$), to resolve larger gradients, medium sized around the the outlet ($\Delta t_2 = 0.2$ and $\Delta t_3 = 0.5$) (see Fig. 4.5) and large anywhere else ($\Delta t_4 = 4cm$) (see Fig. 4.4). Memory requirements were very low ($\approx 20MB$) and computational effort was moderate at 100 iterations and 500s each, resulting in a total run-time of $14h$ per Kn-value.

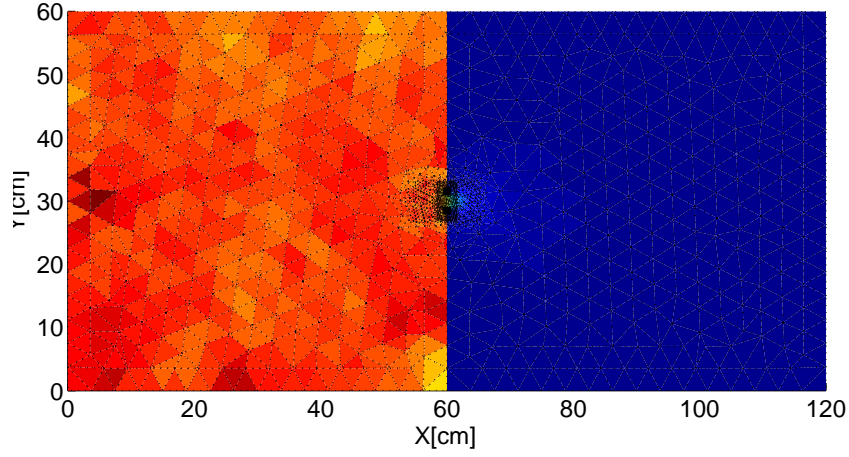


Figure 4.4: Grid for a Knudsen scan of a slit/rectangular orifice ($h/p = 1/20$) generated by the TRIA routine. Two volumes of $60 \times 60 \times 60 \text{ cm}^3$ are connected by a rectangular orifice ($h = 3 \text{ cm}$ and $p = 60 \text{ cm}$). The source was placed at the center of Y and Z at $x = 0.0001 \text{ cm}$ and the pump was set to cover all walls of the low pressure chamber with an absorption coefficient of 100%.

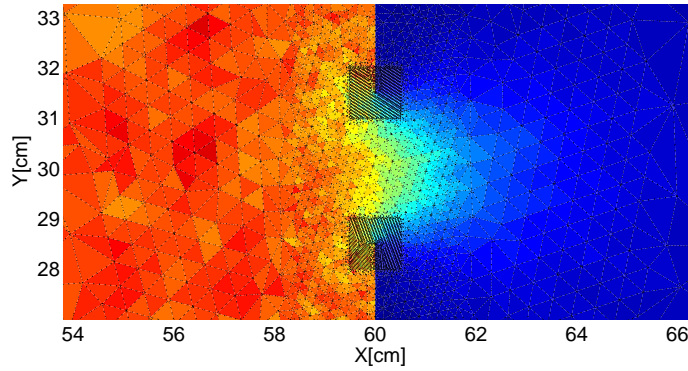


Figure 4.5: Close-Up of the orifice in Fig. 4.4. Three different mesh sizes become apparent: $\Delta t_1 = 0.03 \text{ cm}$ around the edges, $\Delta t_2 = 0.2$ and $\Delta t_3 = 0.5$ around the aperture

4.3.3 Grid for slit created by 3D cartesian mesh

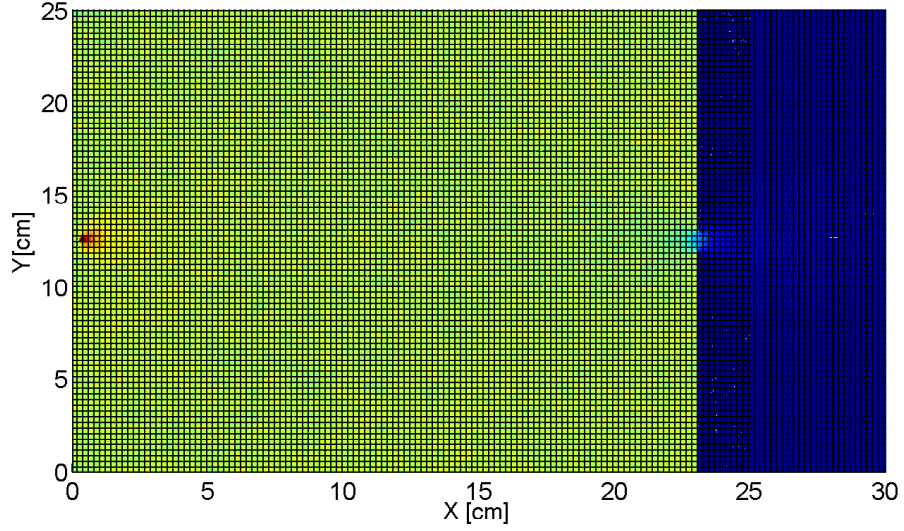


Figure 4.6: Grid for the Knudsen scan of a slit ($h/p = 1/60$) created by a 3D cartesian mesh. A high-pressure volume of $23 \times 25 \times 60 \text{ cm}^3$ is connected to a low pressure volume of $7 \times 25 \times 60 \text{ cm}^3$ by a rectangular orifice of height 1 cm . The source is placed in the left hand chamber, far away from the opening in the center of Y and Z at $x = 0.0001$. The pump is modeled as an absorbing surface in the volume on the right hand side at $x = 30 \text{ cm}$ with an absorption coefficient of 100%.

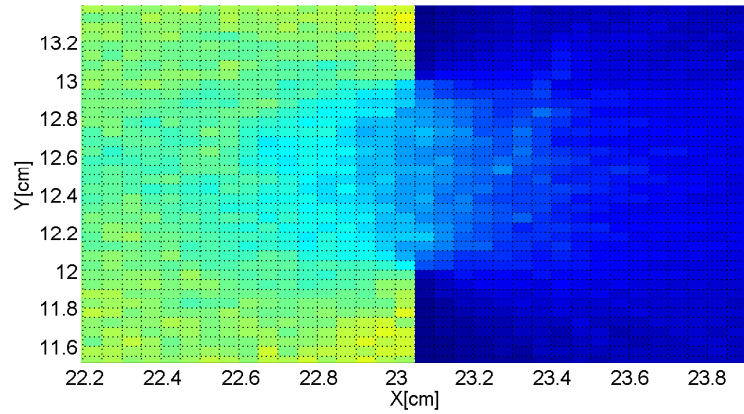


Figure 4.7: Close-up of the orifice area of the grid for the Knudsen scan of a slit created by a 3D cartesian mesh (see Fig. 4.6). The fine mesh resolution was chosen to be $\Delta x, \Delta y = 0.05 \text{ cm}$.

The grid depicted in Fig. 4.6 was also used to model a slit of height $h = 1 \text{ cm}$ and

depth $p = 60cm$. The size of the high-pressure volume was chosen to be $x = 25cm$ and $y = 23cm$ with $X, Y > 20 \cdot h$, to minimize influence of the boundaries on the flow. The mesh-spacing was chosen to be $\frac{\Delta x}{h} = \frac{\Delta y}{h} = 0.05$ for $0cm < x < 25cm$, to resolve the density profile around the outlet (Fig. 4.7), while the mesh-spacing at $25cm < x < 350cm$ was chosen to be more coarse in order to save memory. Memory demands were tolerable at $250MB$ while computational effort was high at around $100 - 150$ iterations and $3000s$ each, resulting in total run-time of up to $5days$ per Kn-value. It should be said, however, that the main reason for high computational cost was the exploration of low Knudsen numbers ($Kn \approx 0.01$), while it was much cheaper for ($Kn > 0.1$) with convergence after only a few ($0 - 30$) iterations.

4.4 Grids with apertures of circular cross-section

Grids with circular cross-section generally demanded more CPU-time per iteration, since the area of the opening was rather small compared to the volume. Therefore particles would spend a lot of time in the high-pressure volume, before hitting the orifice. On the other hand, pressure ratios were always low "by design". For most grids (in fact for all except 4.4.2) rotational symmetry was exploited by rotation along one axis, reducing memory demands quite a bit. The approximation to a circle was done by 60 straight elements. Since EIRENE demands the computational volume to be closed, the boundary at the axis was made specular reflective, or, if not possible, a specular reflective wrap was created around it by an additional surface. Although by strict definition these geometries are not circular orifices but rather an annulus, these "wires" were very small compared to the tube ($\frac{R_{wire}}{R_{tube}} \approx 10^{-4}$) as well as to the cell-size ($\frac{R_{wire}}{\Delta r_{cell}} \approx 10^{-3}$). The distorting influences could be assumed to be negligible, especially since fine gradients occur rather on the outer edge of the orifice, instead of the center.

4.4.1 Grid for tube of finite length with circular cross-section generated by a rotated 2D cartesian mesh

The grid depicted in Fig. 4.8 and 4.9 was used to model circular tubes of finite length ($0cm \leq l \leq 10cm$). The ratio between the diameter d and the sides of the high-pressure volume was always ensured to be large compared to the orifice ($R/d, Z/d > 20$). Again, use was made of the option to split the modeled volume into areas of high resolution in the area around the orifice and low resolution in front of the pump and far away from the orifice. The grid size was set to be $\Delta r, \Delta z = 0.05cm$ in the high resolution area (see Fig. 4.9) giving a resolution of $\Delta \frac{r}{d}, \Delta \frac{z}{d} = 0.05$, and lower elsewhere. The grid was generated using the option implemented in EIRENE for 3D-cylindrical coordinates, the rotational axis was located at $r = 0.0001cm$, and the discretization in R was set to be equidistant (for the fine and coarse resolution

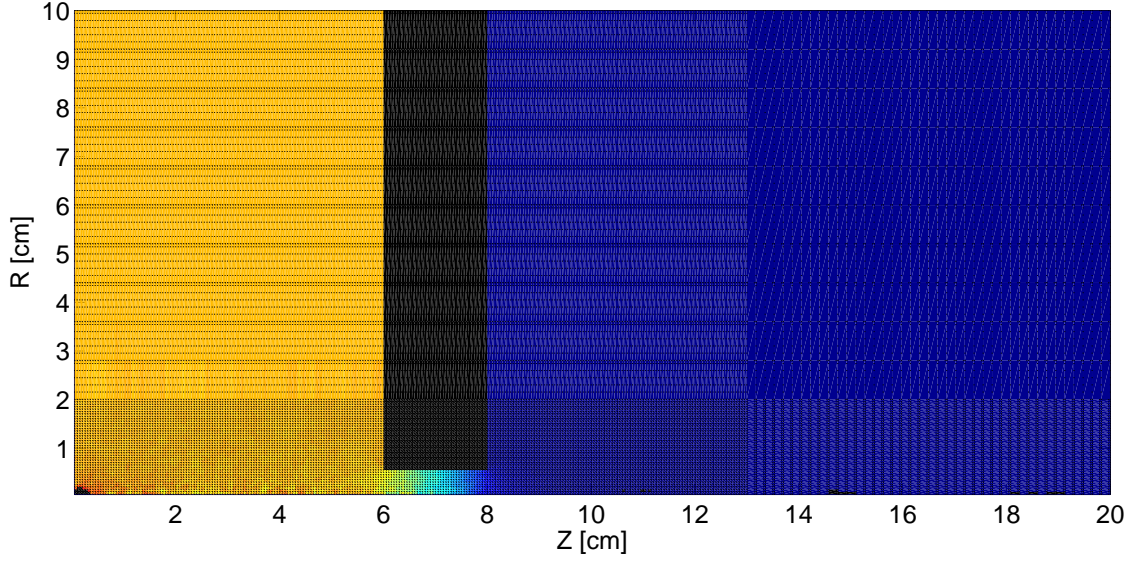


Figure 4.8: The grid for a finite-length circular tube of length $l = 2\text{cm}$ and diameter $d = 1\text{cm}$. The grid was created as a 2D cartesian mesh and rotated around the Z-axis. The high-pressure volume of $2\pi * 10 \times 6\text{cm}^3$ is connected to the low pressure volume of $2\pi * 10 \times (20 - l)\text{cm}^3$ by a circular duct. The source is placed in the left hand chamber at $(z = 0.0001\text{cm}, r = 0.0001\text{cm})$. The pump is modeled as an absorbing surface in the volume on the right hand side at $z = 20\text{cm}$ with an absorption coefficient of 100%, covering the whole wall. Similar grids were generated using the same mesh, varying the length of the tube l .

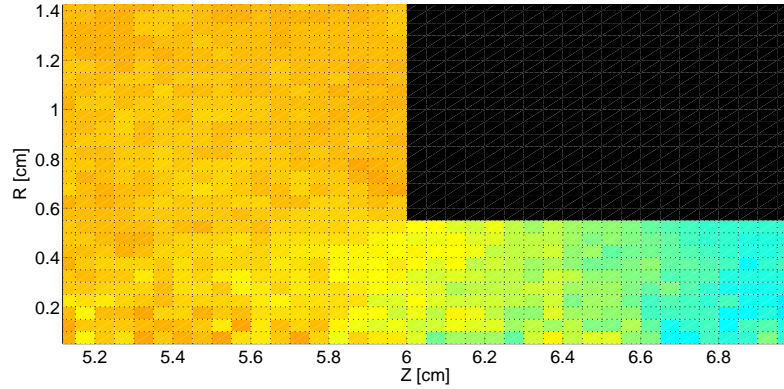


Figure 4.9: Close-Up of the opening of the finite-length circular tube Fig. 4.8. The cell-size was set to be $\Delta r = 0.05\text{cm}$, $\Delta z = 0.05\text{cm}$ in the area around the whole tube

area each). The memory demands were low ($\approx 20\text{MB}$) but demands on CPU time were quite large (100iterations and 3000s each) especially for $l > 1\text{cm}$.

4.4.2 Grid for circular orifice generated by a 3D-Cartesian with an additional surface

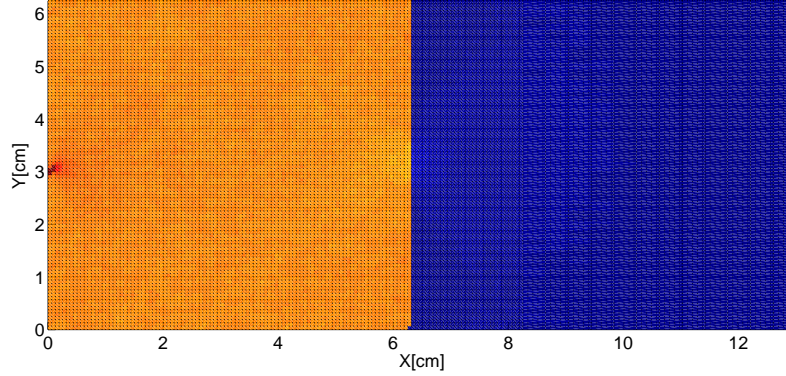


Figure 4.10: A 2D projection of the grid for a circular orifice with diameter $d = 1\text{cm}$, generated by a full 3D-Cartesian mesh with an additional surface. The grid was created as a full 3D cartesian mesh and a diffusely reflective additional surface with a circular hole was set at 6.25cm . The high-pressure volume of $6.25 \times 6.25 \times 6.25\text{cm}^3$ is connected to the low pressure volume of the same size. The source is placed in the left hand chamber at $(x = 0.0001\text{cm}, y = 3\text{cm}, z = 3\text{cm})$. The pump is modeled as an absorbing surface in the volume on the right hand side at $x = 13\text{cm}$ with an absorption coefficient of 100%, covering the whole wall.

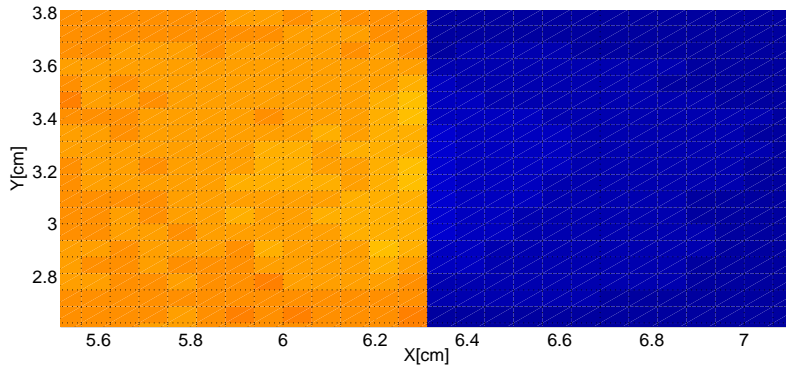


Figure 4.11: Close-Up of the orifice area for the grid in Fig. 4.10. The grid size was set to be $\Delta x = 0.0625\text{cm}$, $\Delta y = 0.0625\text{cm}$, $\Delta z = 0.0625\text{cm}$.

Fig. 4.10 and Fig. 4.11 show a 2D view of the fully resolved 3D-Cartesian grid. The cell-size was $(\Delta x, \Delta y, \Delta z = 0.0625\text{cm})$ in the whole volume for $0\text{cm} < x < 8.25\text{cm}$ (see Fig. 4.11) and coarser elsewhere. An additional surface with a circular orifice and diameter $d = 1\text{cm}$ was set at $x = 6.25\text{cm}$. The high-pressure volume was $6.25 \cdot 6.25 \cdot 6.25\text{cm}^3$, as well as the low-pressure volume. This type of grid

was the most memory demanding, since no symmetries could be used for averaging during calculation. Therefore optimization was done for memory. Keeping cell-size and volume on the minimum memory demands were still around $3GB$. The computational effort was quite moderate at 500s and 100 iterations each resulting in a total run-time of around $14h$.

4.4.3 Grid for a circular orifice generated by a rotated 2D triangular mesh

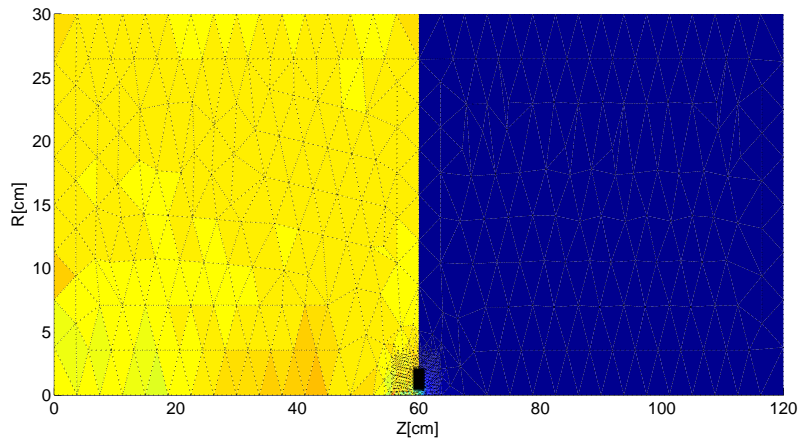


Figure 4.12: The grid for a circular orifice of diameter $d = 3cm$. The grid was created as a 2D triangular mesh and rotated around the Z-axis. The high-pressure volume is $2\pi * 30 \times 60cm^3$ as well as the low pressure volume. The source is placed in the left hand chamber at $(z = 0.0001cm, r = 0.0003cm)$. The pump is modeled as an absorbing surface in the volume on the right hand side at $z = 120cm$ with an absorption coefficient of 100%, covering the whole wall.

Fig. 4.12 and 4.13 show a grid for a circular orifice. It is a triangular grid with variable cell-size, creating two volumes of radius $R = 30cm$ and height $Z = 60cm$ each, connected by a circular orifice of diameter $d = 3cm$. The cell-size around the edge of the orifice is set to be $\Delta t_1 = 0.03cm$ giving a resolution of $\Delta t_1/d = 0.01$. The cell size near the rotational axis was chosen to be coarser at $\Delta t_2 = 0.3cm$ to counteract the radius to cell-volume dependence and to allow for better statistics. Throughout the reservoirs, the cell-size was set to be $\Delta t_3 = 4cm$. The grid proved to be quite memory efficient, though EIRENE, at the current state, is not able to give any output for more then 9999 triangular cells. It is technically possible, however, to extend the code to express output for more cells in principle. The demands on memory were minimal ($\approx 10MB$). The hardest limitation was the computational effort needed, so for lower Knudsen numbers ($Kn < 0.1$) CPU-time had to be set to

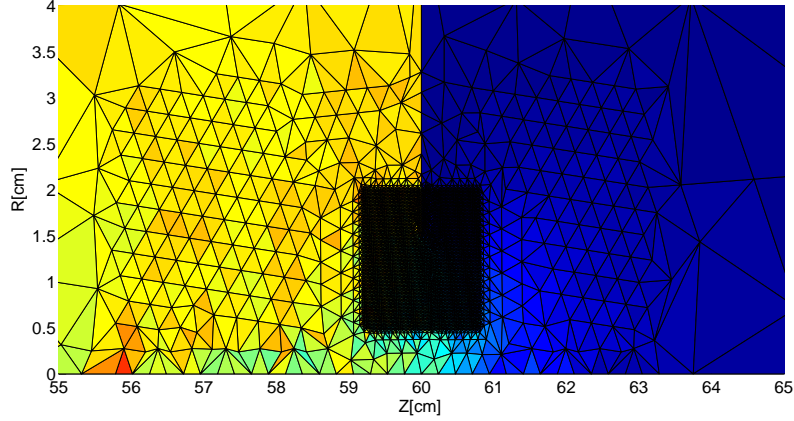


Figure 4.13: Close-Up of the opening of the circular orifice from the grid in Fig4.12. The grid size was set to be $\Delta t_1 = 0.03cm$, $\Delta t_2 = 0.3cm$ in the area around the orifice and $t_3 = 4cm$ everywhere else.

5000s for 100 iterations each, resulting in a total runtime of about a week ($\approx 6days$) for each Knudsen value, to generate a sufficient number of histories.

4.5 Comparison between grid performance

Fig. 4.14 gives a rough overview of the performance of all grids in terms of memory, CPU-time and resolution. Reducing memory by exploiting symmetries had a great impact on memory demands. Grids with a circular orifice tend to be more demanding in CPU time since the particles would spend more time in the high pressure volume compared to the grids with rectangular orifices, before crossing the aperture, simply because the cross section is smaller compared to the surface of the volume. Grids for ducts and pipes of finite length also demanded more CPU time due to interaction with the walls, as well as grids with more cells, because for smaller cells statistical noise was higher. Obviously, for lower Knudsen numbers and therefore higher collisionality, demands on CPU were higher as well. As for the ratio between the dimensions of the high pressure volume and the dimensions of the aperture, the influence of the volume boundaries on the result were kept minimal while maintaining computational efficiency. The triangular grids proved to be the most memory efficient (although a bit slower), since highly resolved areas could be defined locally, whereas the cartesian grid grids allowed for only two different resolutions per dimension. On the other hand, triangular grids were limited by the maximum number of cells $N_{cell} < 9999$.

Section in this chapter	cross-section	TRIA/Cartesian/Cartesian3D	Memory Demands	CPU demands	Resolution
Sec.:5.2.1	rectangular	TRIA	low	low for linear runs	low
Sec.:5.2.2	rectangular	Cartesian	moderate	high	0.05
Sec.:5.2.3	rectangular	TRIA	low	moderate	0.01
Sec.:5.3.1	circular/rotated	Cartesian	moderate/low	high	0.05
Sec.:5.3.2	circular	Cartesian3D	Very high	moderate	0.0625
Sec.:5.3.3	circular/rotated	TRIA	low	very high	0.01

Figure 4.14: A Comparison between the performance of all grids. The resolution is the ratio between the cell-size $\Delta x, \Delta y, \Delta z, \Delta t$ of the finely meshed area and the typical dimension D ($\frac{\Delta x y z t}{D}$).

4.6 Uncertainties

For a verification it is essential to give a measure of the uncertainties of the performed calculations. Critical sources of possible errors were choosing the point of convergence, influence of the grid and, of course, statistical errors when dealing with Monte-Carlo methods.

4.6.1 Convergence

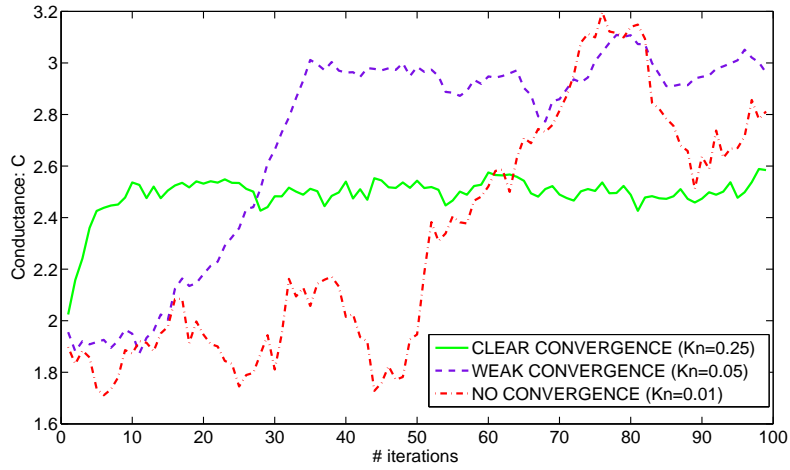


Figure 4.15: Example for convergence(3D slit)

Although great care was taken to ensure convergence, it was not always clear when convergence was reached. Especially in cases with high collisionality, build up to equilibrium could need a lot of CPU time per iterations, as well as many iterations, so the convergence would be slow and in some cases not obvious. For high Knudsen numbers ($Kn > 0.1$) convergence was reached quickly, usually within 30 iterations and often even less. Fig. 4.15 shows examples displaying typical behavior. A point at which convergence was assumed was then identified and an average was taken over all following results. This procedure showed to yield a standard deviation, slightly larger than the statistical error σ calculated from the Monte Carlo algorithm. This difference is a consequence of the successive linearization scheme in particular the finite cell-size, which amplified the statistical error and caused a slightly fluctuating equilibrium. Also, each set-up showed specific convergence behavior which had to be verified each time.

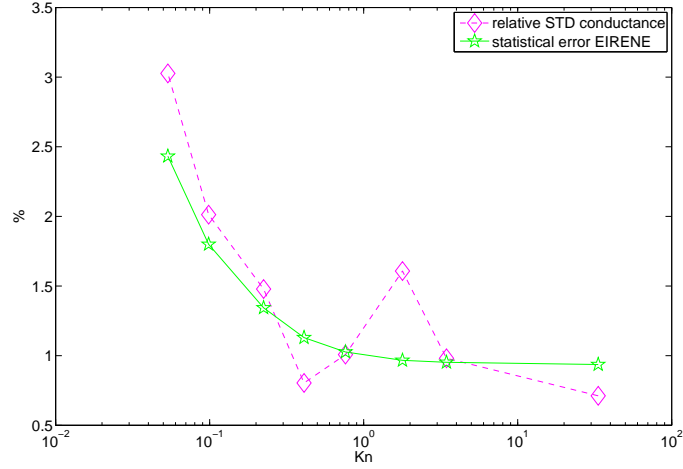


Figure 4.16: The statistical error, calculated by EIRENE, averaged over all cells as well as the standard deviation of the converged conductance is plotted against the Knudsen number. The values correspond to a circular tube with length to radius ratio $L/R = 1$ for 3000s for each iteration.

4.6.2 Statistical error

For the error in the calculation of conductance, the relative standard-deviation of all converged non-linear runs is taken. At fixed CPU time, the number of particle histories decreases for lower Knudsen-numbers because more collisions demand more computational effort. The number of histories, also depends on the actual conductance. In Fig 4.16 the relative standard deviation of conductance is plotted against the Knudsen number and shows typical behavior for fixed CPU time and the maximum standard deviation was always 3 – 5% for low Knudsen numbers. The standard deviation of the converged conductance surpassed the statistical error for low knudsen numbers.

4.6.3 Influence of the grid

The cell-size turned out to be a limiting factor in this validation. In order for the flow to develop properly, all gradients must be resolved correctly. To ensure high enough resolution, cell-size should not surpass the mean free path length. Unfortunately with increased number of cells, demands in memory and CPU time increased as well. When using too few cells, calculations would give the correct value for conductance until a Knudsen number was reached, where the mean free path length was smaller than the cell-size/ D -ratio (D is the typical dimension as defined in Sec. 2.2) and then break down. This can be seen from Fig. 4.17, where the same geometry was scanned with different cell-size/ D -ratios. They are marked in corresponding color

on the Knudsen scale. When using too many, memory demands increased, often beyond hardware limitations and when cells were too small, the statistical noise was high and therefore necessary CPU-time was increased as well. Hence, finding a reasonable compromise was important.

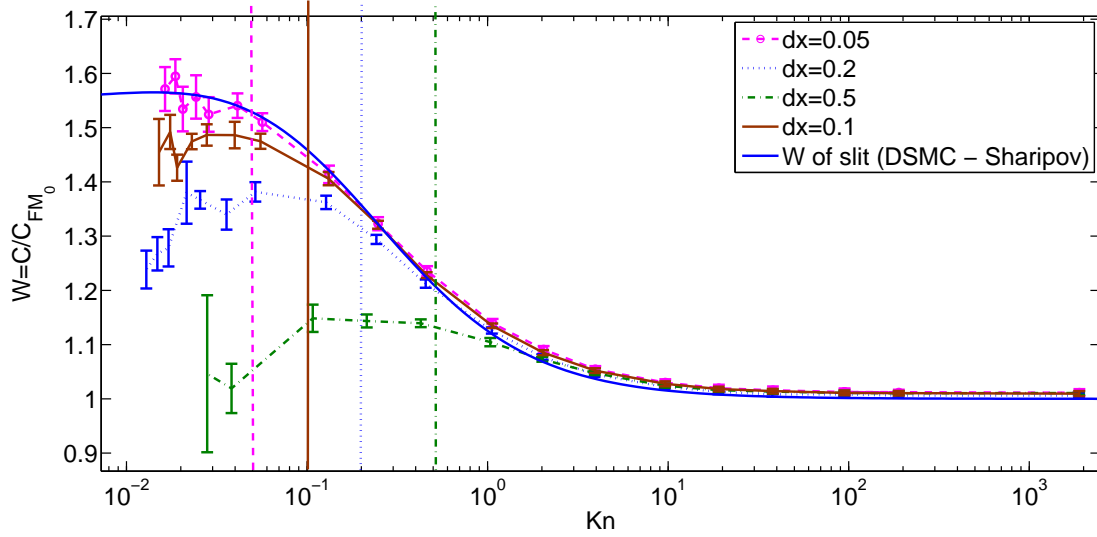


Figure 4.17: Cellsize-dependence

Additional uncertainty comes along all toroidally rotated grids, since in those cases the cell-size varies with R^2 and the cells close to the rotational axis are therefore extremely small. This also results in a higher statistical error and in some cases has effected the outcome of the results. Although the differences for most cases were negligible, this needs to be kept in mind.

Also, because larger reservoir volumes needed more memory and CPU-time, the volumes were set to a size, where the influence was tolerable while still being computationally efficient. This usually resulted in a slightly increased finite pressure ratio and a slightly increased free-molecular conductance, than what would have been expected by Eq 2.6. Theses effects were the strongest for rectangular ducts but the off-set was always kept below 1.5%.

Chapter 5

Results

For the validation of the distributions calculated by EIRENE, the conductances calculated for the grids described in the previous chapter have been evaluated and compared to well documented cases in the literature. All simulations were run using D_2 with correct viscosity, while neglecting energy levels from inner degrees of freedom. Definitions of Knudsen numbers have been made consistent with the convention used for this thesis (See Eq. 2.5). The conductance for flow into vacuum of a slit, a circular orifice and circular tubes of length-to-diameter-ratios between $0.05 < l/d < 10.0$ has been compared for $\text{Kn} > 0.05$. The conductance for flow at finite pressure-ratio of a short tube of length/diameter-ratio $l/d = 0.5$ compared for $\text{Kn} > 0.1$. Finally the implemented BGKES extension has been tested, although not yet fully validated.

5.1 Free molecular length scan of a slit

In the beginning of the validation of EIRENE, the validity of the resulting conductance was checked for the free-molecular regime, for the case of slits of different lengths Fig. 5.1, using the grid from Sec. 4.3.1. The results were compared with different formulas to calculate conductance namely using the analog from electric conductance Eq. 2.9, applying the original formulas by Knudsen Eq. 2.8 and Smoluchowski Eq. 2.10 for infinitely long slits, and a more correct numerical treatment performed by Clausing, found in the literature [40]. The agreement with the Clausing data was found to be within 0.3% (except for $l = 10m$, where agreement was found to be in between 8% but right between the Clausing and the Smoluchowski equation), while the statistical error σ calculated by EIRENE was around 0.8%. The agreement with Eq. 2.9 using the Smoluchowski formula was the worst for short lengths, but for the very long duct ($l = 10m$) it agreed with the Clausing data as well as the EIRENE results, while the Knudsen-formula failed and underestimated conductance by more than 50%. This surprising effect of two errors co-occurring to give a more realistic result has already been pointed out by Clausing in his original paper [21]. Meanwhile, there have been carried out more accurate numerical calculations, for example Santeler's work [41], using the Clausing integral equation,

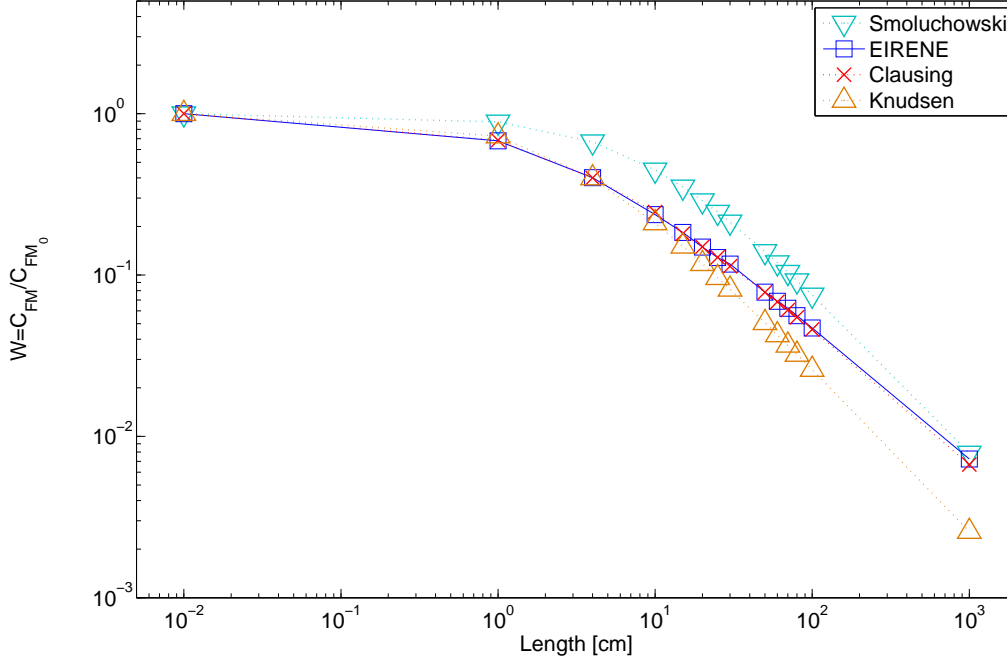


Figure 5.1: Scan of slits of various length-to-height ratios ($h = 1\text{cm}$; $0 < l < 1000\text{cm}$, width: $p = 10.366\text{m}$) in the free-molecular regime. Theoretical values are plotted for comparison. The Conductance calculated by EIRENE agrees very well (within 0.3%) with the theoretical value given by Clausing [40].

which shows the same results as Clausing's, only with higher accuracy up to 0.03%. Although highly accurate, these numerical solutions have only produced tabulated data for fixed geometrical properties, making them quite unhandy for the calculation of conductance for complex 3-dimensional structures.

5.2 Knudsen scan of a slit

A Knudsen scan was performed for a slit (see Fig. 5.2) using the grid in Sec. 4.3.3. The agreement with the DMCS-results provided by Felix Sharipov Eq. 2.15 was very good ($< 2\%$) for all Knudsen numbers ($\text{Kn} > 0.02$) even up to the continuum regime. A slight overestimation for high Kn could be detected, probably resulting from the finite reservoir volume. For $\text{Kn} < 0.05$ the results obtained, showed some level of scatter resulting from larger statistical error.

A second Knudsen scan was performed for a slit (see Fig. 5.3) using the grid in Sec. 4.3.2. The agreement was fair ($< 5\%$) for $\text{Kn} > 0.05$ and good for $\text{Kn} < 0.1$ ($< 3\%$). For lower Knudsen numbers the conductance was systematically underesti-

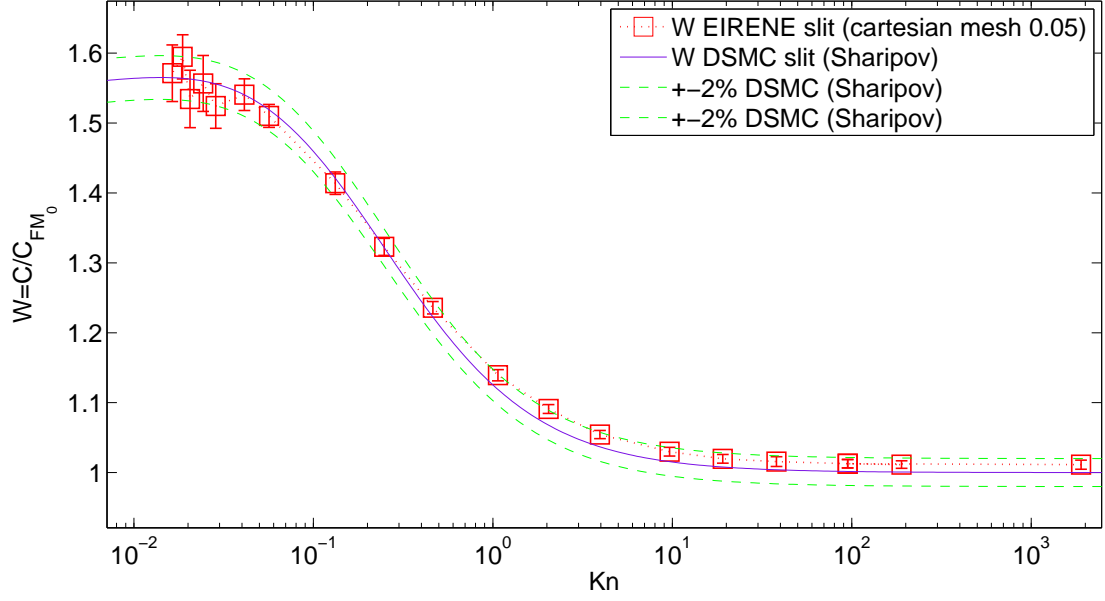


Figure 5.2: Knudsen scan of a slit (height $h = 1\text{cm}$, width $p = 60\text{cm}$) on a grid with a cartesian mesh. The agreement was within 2% up to the continuum regime ($\text{Kn} > 0.02$).

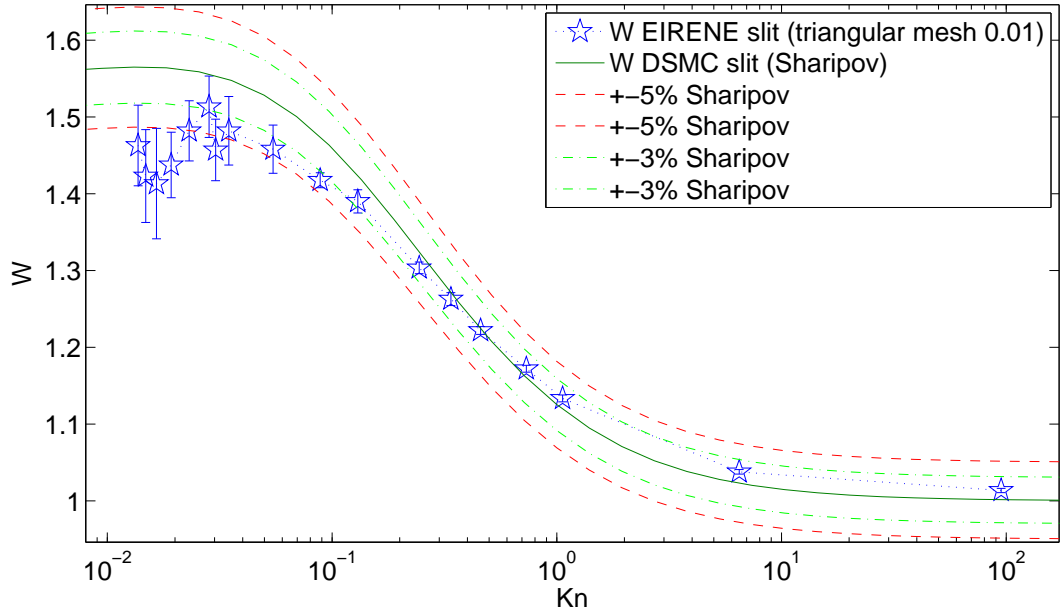


Figure 5.3: Knudsen scan of a slit (height $h = 3\text{cm}$, width $p = 60\text{cm}$) on a grid with a triangular mesh. The agreement was ($< 3\%$) for $\text{Kn} > 0.1$ and ($< 5\%$) for $\text{Kn} > 0.05$.

mated, indicating insufficiency of the grid resolution. Since influences from the finite reservoir volume could not be totally neglected, the pressure ratio was $\frac{P_2}{P_1} = 1.3\%$ and a slight overestimation for high Kn was also observed. Although the grid included a fine resolution area around the edges of the slit, the medium sized resolution surrounding it, may have prevented an accurate calculation of the flow profile and therefore an early break down as indicated in Sec. 4.6.3. Unfortunately, because the current version of EIRENE is unable to produce output for more than 9999 triangles, a finer grid resolution could not be tested.

5.3 Knudsen scan of a circular orifice

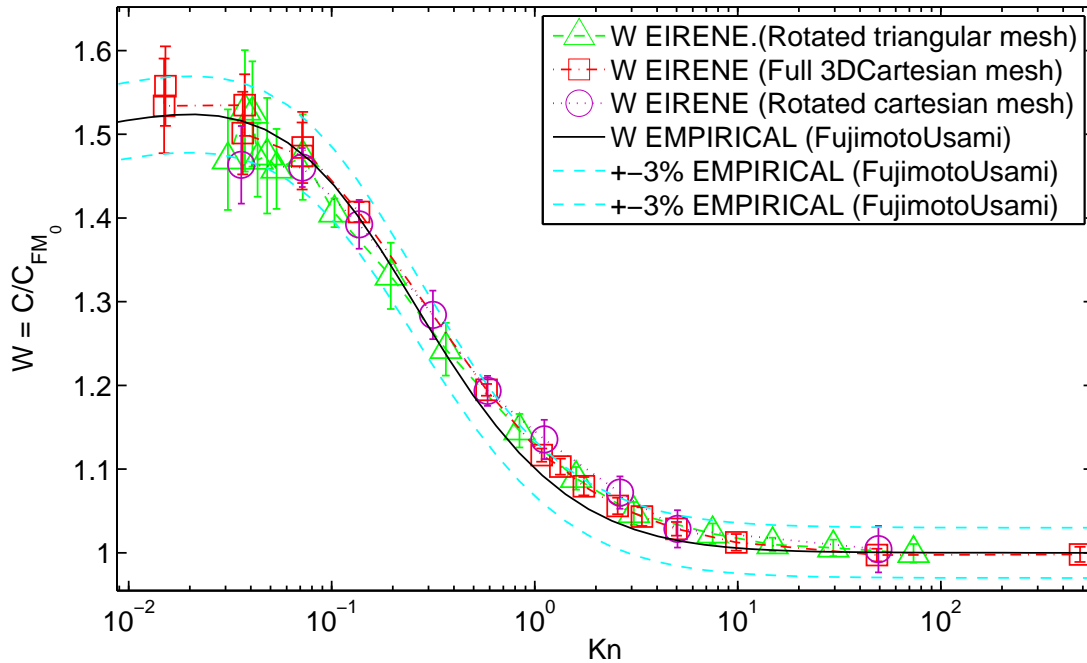


Figure 5.4: Knudsen scan for circular orifice (radius $R = 0.5cm$) performed by 3 different mesh types. Agreement in between the mesh types is very good for $Kn > 0.1$. Overall agreement with the empirical formula Eq. 2.14 by Fujimoto and Usami was within 3% for $Kn > 0.05$.

Since EIRENE is highly flexible in generating 3-dimensional meshes, several options to model a circular orifice have been found to produce good results and each mesh-type has its own advantages. A comparison has been made (Fig. 5.4) between the option of a rotated triangular grid (Sec. 4.4.3), a cylindrical grid (Sec. 4.4.1) and a fully resolved 3D cartesian grid including an additional surface with a circular hole in it (Sec. 4.4.2). Additionally, the proposed formula (Eq. 2.14) by Tetsuo Fujimoto

and Masaru Usami [6] has been plotted, even though it is a formula derived from experimental data and therefore only includes a approximation for circular orifices with length $l = 0$. The comparison shows absolute agreement within statistical error between the grids and a good agreement with the empirical formula ($< 3\%$ for $\text{Kn} > 0.05$). In the transition regime ($0.5 < \text{Kn} < 10$) the conductance seems to be systematically overestimated by a few percent. It can be seen that the cylindrical grid and the triangular grid give scattered results for $\text{Kn} < 0.05$, yet indicating a slight underestimation of the "overshoot", a local maximum between the viscous and inviscid regime, with slightly higher conductance than what the Euler equation predicts (See Fig. 2.4). Surprisingly the result of the fully resolved 3D-cartesian grid seems to resolve the "overshoot" and remains to produce reasonable results even though the cell-size was the coarsest and should not have allowed resolution for $\text{Kn} < 0.0625$.

5.4 Circular Pipe: Lengthscan

Due to the problems with the other grids (memory demands, limited cell-number and CPU time efficiency), the cylindrical grid (Sec. 4.4.1) was chosen to perform a comparison with empirical data for Knudsen scans of circular pipes with different length-diameter ratio $L/2R$ (see Fig. 5.5). The agreement is good, varying slightly for each pipe-length. Very short pipes ($L/D < 0.2$) were found to have the weakest agreement ($< 4 - 6\%$), overestimating in the transition regime ($0.5 < \text{Kn} < 10$) and underestimating in the continuous regime ($\text{Kn} < 0.5$). This might be due to poor resolution of the pipe length, yielding only 1,2 or 4 cells over the whole pipe length. For medium length pipes the agreement was found to be good ($\approx 3\%$) for $\text{Kn} > 0.05$. Generally it was within standard deviation but with a trend for underestimation at lower Knudsen numbers $\text{Kn} < 0.1$.

The longer pipes with $L/2R > 2.0$ showed again only fair agreement ($< 5\%$) for $\text{Kn} > 0.05$ and tended to underestimate over all Kn . Underestimation for long pipes could be a result of large fluctuations due to weak statistics and therefore poor convergence, since ducts of finite length show increased collisionality and consume generally more CPU time.

5.5 Conductance at finite pressure ratios

An attempt was also made to compare conductances at finite pressure-ratios $\frac{P_2}{P_1}$, on the cylindrical grid 4.4.1 with $L/2R = 0.5$. To vary the pressure ratio, the absorption coefficient of the pump was varied for each scan. Because there was no option to stabilize the pressure ratio between the volumes at a steady value, averages had to be taken. The pressure ratio would not only vary from iteration to

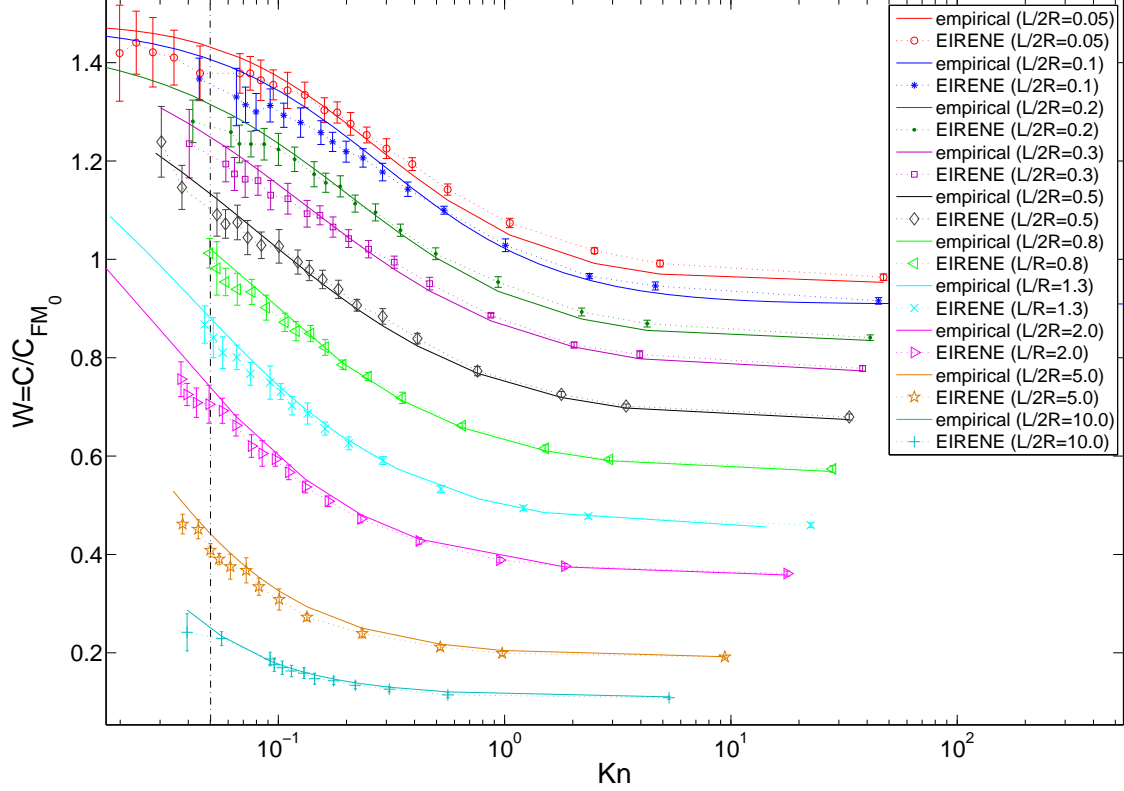


Figure 5.5: Knudsen scan for circular tubes of different L/R ratio ($R = 0.5\text{cm}$; $0.05\text{cm} < L < 10\text{cm}$). The agreement was generally between 2 – 6%, depending on L/R , mostly within standard deviation for $\text{Kn} > 0.05$. The dotted grey vertical line marks the Kn where cell-size \approx mean free-path.

iteration, but also within each scan. For lower pressure ratios, the variation was not as wide, but still significant as can be seen in Fig. 5.6, but in particular the high pressure ratio would vary from 30% for high Knudsen values to around 65% for the lowest Knudsen value. Non the less the data shows good agreement with the data by Fujimoto and Usami (see Fig 5.7) up to a Knudsen number of $\text{Kn} > 0.1$ and for the data from Varoutis [9] the agreement is always within 4%.

Because of the great uncertainty involved in averaging the pressure ratios, an additional comparison was made with a semi-empirical formula from Sreekanth Eq. 2.16 in Fig. 5.8. Although Eq. 2.16 is claimed to be valid for $0.1 < \text{Kn} < 1.7$, the formula has been shown in [9] to overestimate for low pressure ratios $\frac{P_1}{P_2}$ and small Knudsen numbers. Since Eq. 2.16 is depending on the pressure-ratio, the actual value from each Knudsen value was used for the evaluation, and pressure was only averaged for each Knudsen value. The data shows good agreement with the empirical formula Eq. 2.16 for $\text{Kn} > 0.1772$ within less than 5%. The value for very

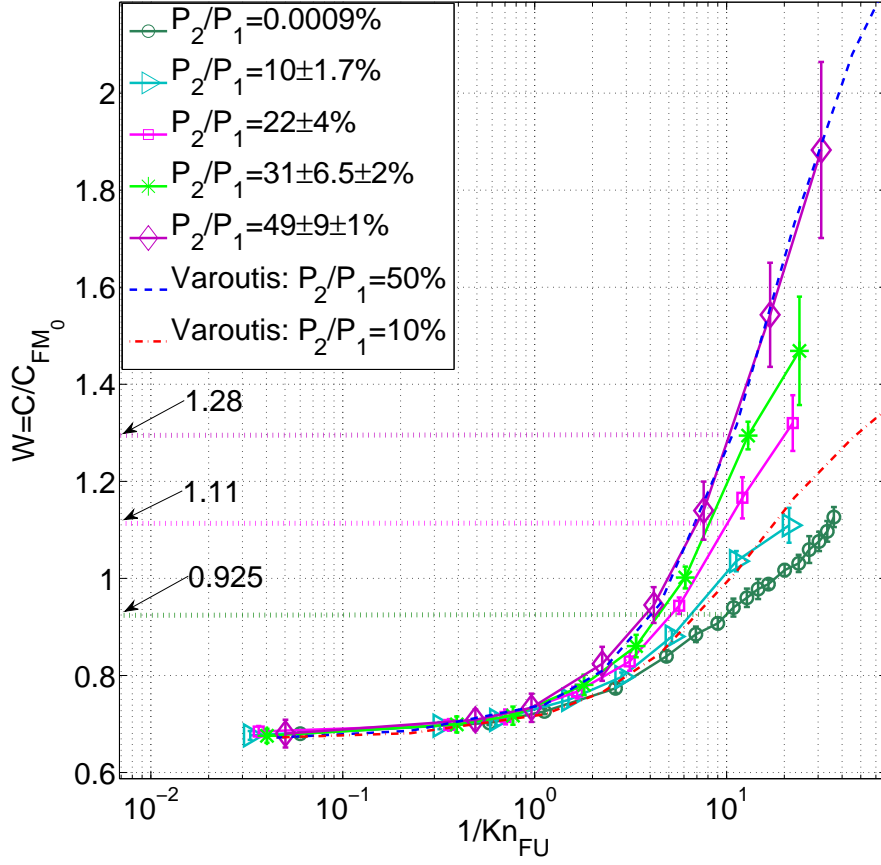


Figure 5.6: Normalized conductance ($W = C/C_{FM_0}$) calculated by EIRENE is plotted against Kn_{FU} for $L/R = 1$. Several pressure ratios (P_2/P_1) are depicted. The error given for each pressure consists of the absolute standard deviation of the scan, followed by the absolute standard deviation within each iteration for the lowest Kn value, if it was larger than 1%. Additionally, selected W values are highlighted for $1/\text{Kn}_{FU} = 10$ from the scans with average pressure ratio $P_2/P_1 = 0\%, 22\%$ and 49% , corresponding to the marked values in Fig. 5.7. (Please note that the convention for the Knudsen number $\text{Kn}_{FU} = \frac{1}{2}\text{Kn}$ by Fujimoto and Usami [6] is applied in this graph for easier comparison with their results!). Also two scans from [9] have been included, for $P_2/P_1 = 10\%$ and 50% . The agreement is very good for $1/\text{Kn}_{FU} = 20$, corresponding to $\text{Kn} > 0.1$. The disagreement is always less than 4%.

low pressure ratio, showed the worst agreement, although the pressure ratio was the most stable and comparison with the more recent data [6] showed very good agreement up to $\text{Kn} > 0.05$ (see Fig 5.5). This is in accordance with [9] and can be explained by the empirical nature of Eq. 2.16, where low pressure ratios were not taken into account. For the comparison a normalized conductance $W(1 - \frac{P_2}{P_1})$ has

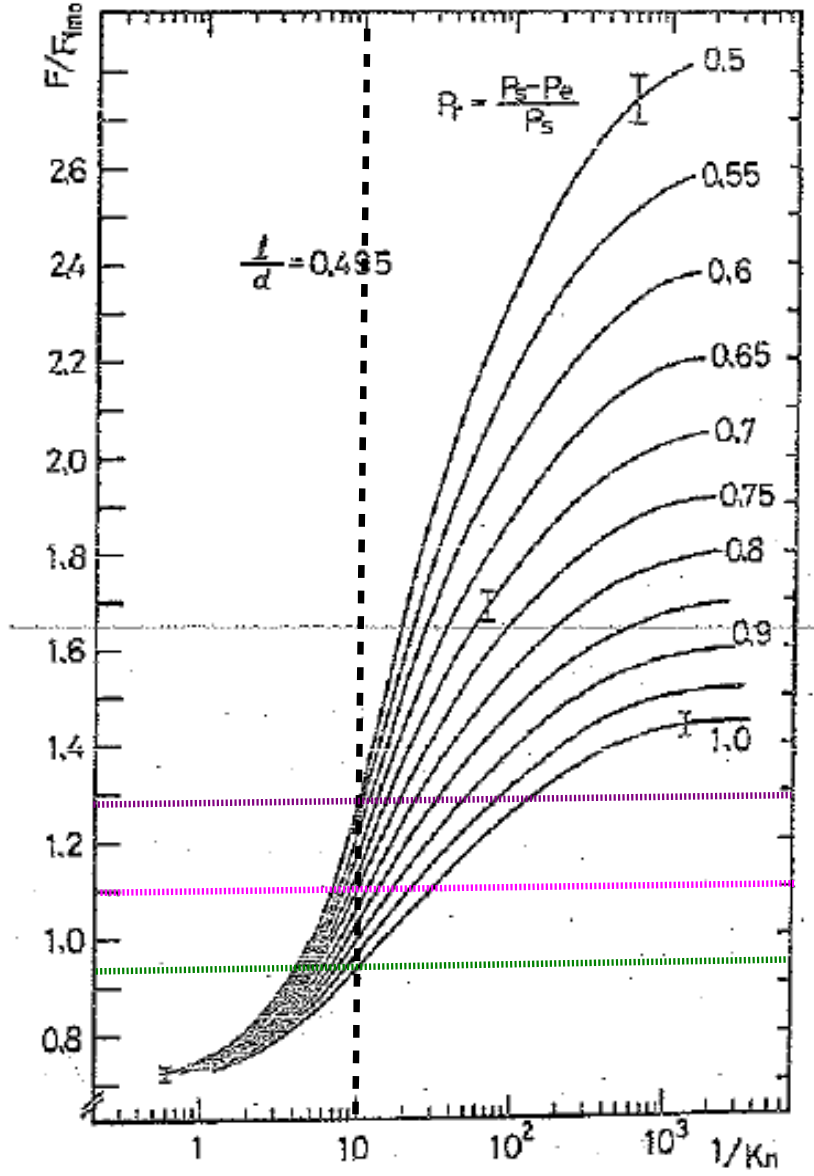


Figure 5.7: The original plot of a Knudsen scan for different pressure ratios $\frac{P_1 - P_2}{P_1}$ by Fujimoto and Usami taken from [6] for a short pipe with $L/R = 1$. Additionally the corresponding values for $P_2/P_1 = 0\%, 22\%$ and 49% are highlighted for easy comparison with Fig. 5.6.

been applied, corresponding to the convention used by Varoutis [9].

$$W(1 - \frac{P_2}{P_1}) = \frac{CP_1/(P_1 - P_2)}{C_{FM_0}} \quad (5.1)$$

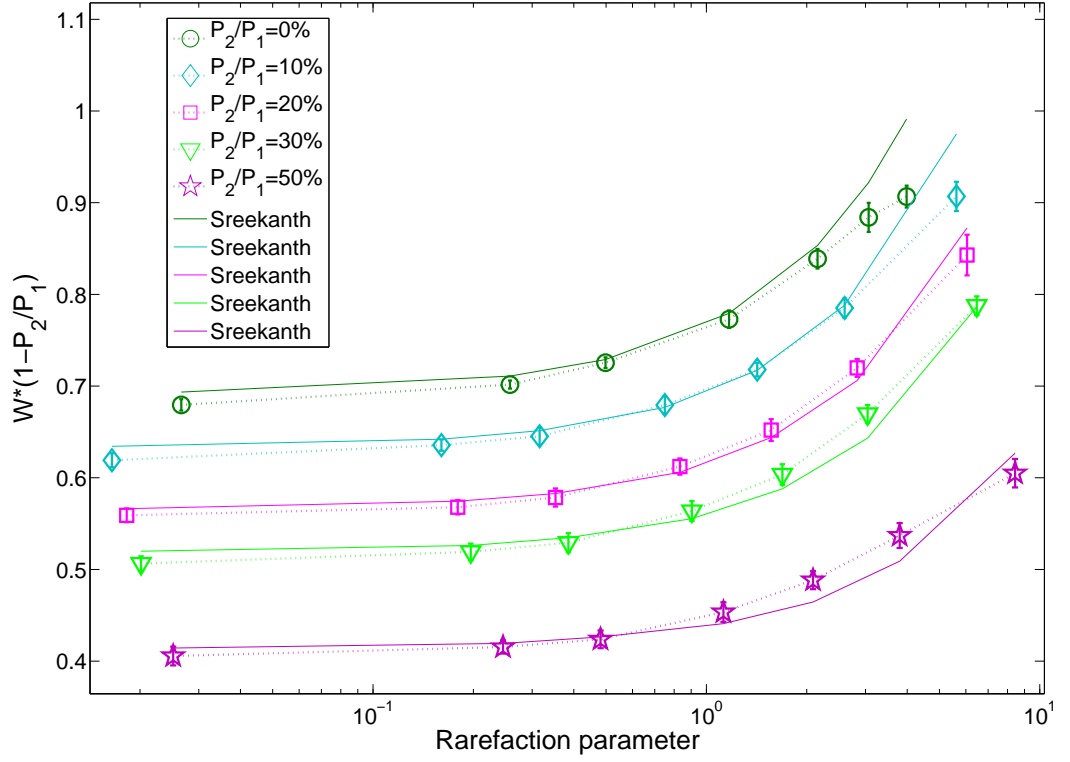


Figure 5.8: Results of EIRENE (marked with symbols) for a slit ($L/R = 1$) are compared against the empirical formula by Sreekanth 2.16. A normalized conductance $W(1 - \frac{P_2}{P_1})$ is plotted against the rarefaction parameter $\delta = \frac{\sqrt{\pi}}{2} \text{Kn}^{-1}$ for easier comparison with [9]. The agreement is within 5% for $\delta < 5$ or $\text{Kn} > 0.1772$, except for low pressure ratios. The legend gives the values of the averaged pressure for each scan, to allow a comparison with Fig. 5.6, but Eq. 2.16 is evaluated using the actual corresponding pressure ratio for each Knudsen value.

The scans were computationally quite expensive, because of high collisionality in both volumes and longer histories due to lower pumping, which resulted in very poor performance for $\text{Kn} < 0.1$ and weak convergence, even for long CPU time ($2000s \times 100\text{iterations}$).

5.6 The BGKES extension

The EIRENE-BGK code was successfully extended to include the BGKES collision model described in Sec. 3.4. A comparison has been made also including the case where the free parameter b (see Eq. 3.31) was chosen to replicate the results from the BGK model ($b = 0$). The conductances calculated by the new collision model were able to replicate the conductance calculated by the currently implemented model, within standard deviation (see Fig. 5.9 and 5.10), indicating the correctness of the extension, but no improvement in accuracy of conductance was found.

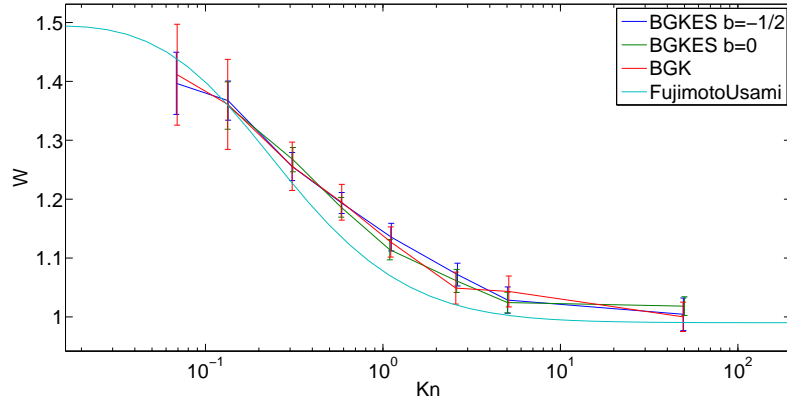


Figure 5.9: Comparison of BGK and BGKES extension, for a circular orifice ($R = 0.5cm$), the pressure ratio was $\frac{P_1}{P_2} = 0.0013$

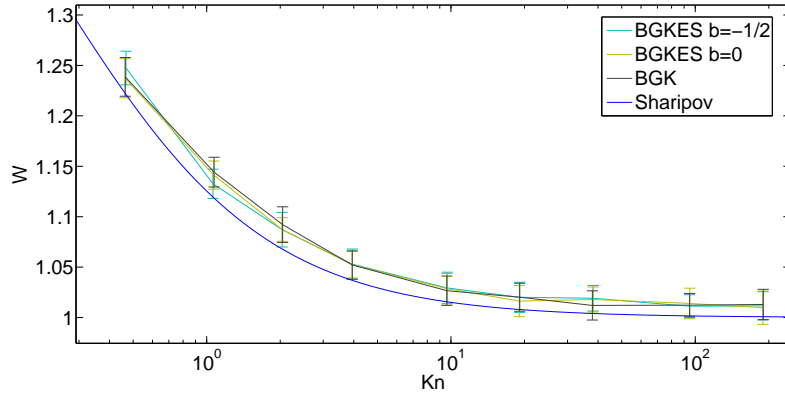


Figure 5.10: Comparison of BGK and BGKES extension, for a slit ($h = 1cm$, $P = 60cm$) the pressure ratio was $\frac{P_1}{P_2} = 0.02$

Unfortunately finding a well documented temperature profile for flows into vacuum to compare with was difficult, since the temperature profiles are highly depended on any finite background pressure [9]. Thus so far only a qualitative statement can be

made. The temperature profiles produced, showed only little differences for the free parameter $b = -\frac{1}{2}$, resulting from a realistic Prandtl number, while the temperature profile of the current model was reproduced for $b = 0$, as expected (compare Fig. 5.12, 5.11). The differences between the temperature profiles are within statistical uncertainty, although a slight difference in shape can be observed in Fig. 5.11. A better test case needs to be examined for a final validation of the new model for a correct Prandtl number ($\text{Pr} = 2/3$), and it might give a more realistic calculation of the temperature distributions for future applications.

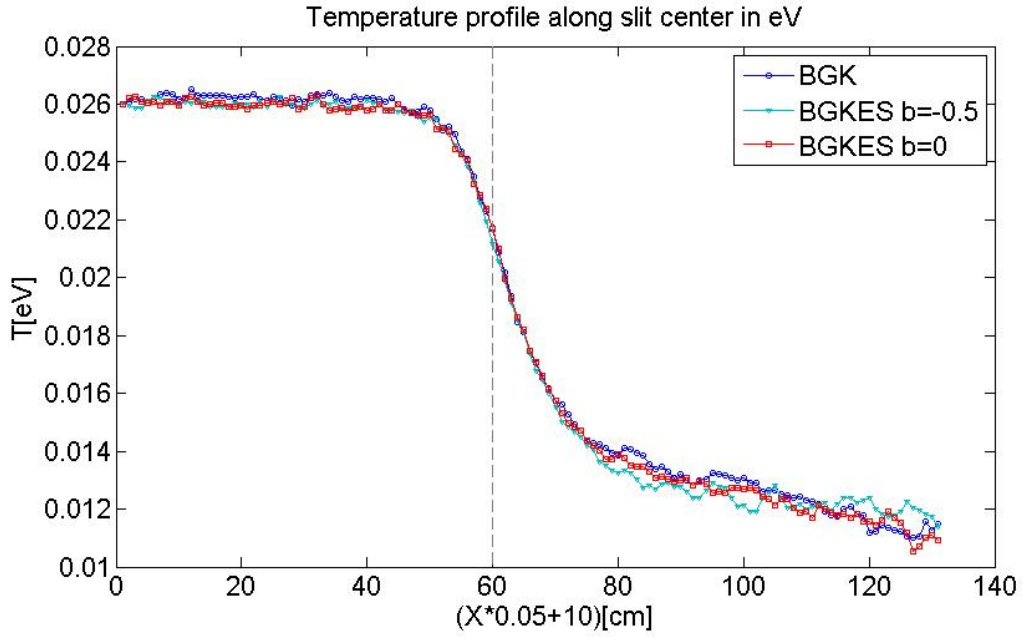


Figure 5.11: The temperature profile along the mid-axis of a slit ($h = 1\text{cm}$, $p = 60\text{cm}$), generated by the cartesian grid described in 4.3.3. The agreement between the BGKES with $b = 0$ and the BGK is very good. The BGKES approximation with $b = -0.5$ shows a slightly different shape but within statistical error. Since computational time was scarce, statistical error is large far away from the orifice. Background density in the downstream volume is not negligible and has a very strong effect on the temperature profile.

The efficiency of the new model is somewhat worse than of the current model, using about 20% as much CPU time for the same number of histories, but the current extension is not yet optimized for computational efficiency. Another problem occurred for the transformation when the free path lengths was sampled to end in a "dead" (or empty) cell. The temperature there is read as zero, and the transformation matrix will then always return a zero velocity, causing the particle to "freeze", and stop the whole run. This problem was solved by skipping the transformation and thereby assuming regular BGK-like distribution in the "dead" cells.

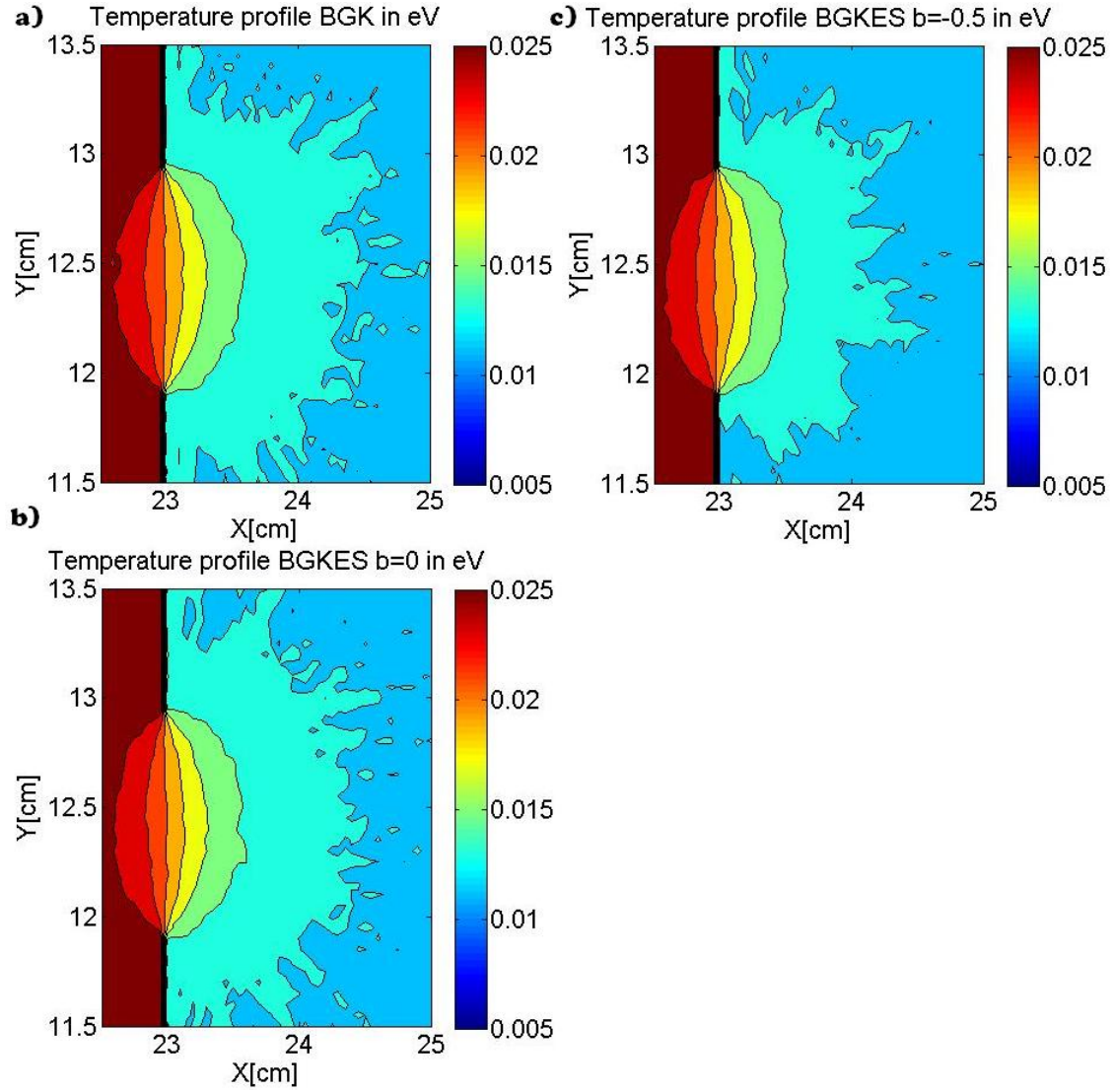


Figure 5.12: Temperature profiles for a slit ($h = 1\text{cm}$, $P = 60\text{cm}$) in the BGK approximation (**a**), in the BGKES approximation, with $b=0$ (**b**), in the BGKES approximation, with $b = -1/2$ (**c**). A slight difference can be observed, but all within statistical noise. The profiles are taken at $\text{Kn} = 9.5$ or $\delta = 0.093$, the pressure ratio was at $\frac{P_1}{P_2} = 0.02$

Chapter 6

Summary and Conclusion

In magnetic confined fusion experiments, neutral particles are essential in controlling the plasma properties. Since under high vacuum condition, especially in the transition between the fluid and the collision-less limitss, analytical approaches fail in calculating correct neutral particle distributions and numerical approaches are required. Since the numerical calculation of flows in complex 3 dimensional structures under high vacuum conditions is impracticable even with modern day computer power, alternative methods are being explored.

In this thesis the Monte Carlo code EIRENE has been benchmarked for the calculation of conductances against data obtained from experiments as well Direct Simulation Monte Carlo (DSMC) calculations. EIRENE is a Monte Carlo solver of the Boltzmann equation in the well validated BGK approximation, where the complex collision integral of the Boltzmann equation has been replaced by a term, assuming local relaxation to a drifting Maxwellian distribution.

The resulting comparison with the data obtained from experiments as well as DSMC calculations proved to yield satisfying results for flow into vacuum for Knudsen numbers up to the continuum regime $Kn > 0.05$. The maximum deviation was found to be 5% and usually even less. It can partly be attributed to inevitable external factors, like the finite reservoir volume or slow convergence. Computation time highly depended on the particular case but results could be aquired within a reasonable amount of time. For $Kn > 0.1$ computation time was between a few hours and a day, for lower Kn it was up to one week in extreme cases. For flow at finite pressure ratio, agreement was found to be within 5% as well, for $Kn > 0.1$. It can be confidently said that, given the proper grid resolution and computational resources, conductances calculated by EIRENE will be in general accurate to a few percent. However, it should be noted, that EIRENE was originally not designed for the calculations attempted in the continuous regime at low knudsen numbers $Kn < 0.1$ but still provides good results.

As part of this thesis, the code was extended with a new collision model, to solve the Boltzmann equation in the BGKES approximation. The resulting conductances showed no difference to the current model, but the temperature profiles appeared to be more realistic. A thorough validation of the temperature profiles, produced by the

extended code has yet to be done. A more realistic determination of temperature distributions of neutral particles could be very useful for to determine the heat transports in a Divertor configuration. Overall the feasibility to include transformed collision models has been shown and might even be extended to include other similar models.

Finding appropriate meshes for the calculations and optimzing them in terms of memory and computational efficiency was crucial. Grid resolution showed to have an great impact on the performance of the calculation and limit the range of Knudsen numbers where a valid result can be expected. For low grid resolution, higher flows at higher densities could not appropriately be resolved and for resolutions too high, the calculations became computationally too inefficient. Since for each grid, the specific conditions had to be found, investigations of the properties of the grids were necessary, to minimize external effects. The grids were documented in great detail and represent an optimum in resolution, computational efficiency and accuracy.

As EIRENE is considered work-in-progress by the authors D.Reiter et al. from the Institute of Energy Research, Forschungszentrum Jülich GmbH, it is constantly extended and validated, which is part of the concept of high flexibility. Although the high flexibility makes EIRENE extremely useful for a multitude of applications, especially in fusion research as the neutral-plasma coupled version B2-EIRENE, it comes at a cost of complexity. Learning how to use EIRENE properly and debugging the version was therefore a major part of this thesis.

As a conclusion it can be stated that in combination with the TRIA routine, EIRENE represents an accurate and computationally efficient tool for the calculation of particle transport in 3 dimensional structures of almost arbitrary complexity. Since a parallelized version has been recently released, the efficiency will increase even further, making EIRENE a convenient tool for calculating vacuum gas flows.

Chapter 7

Appendix

7.1 Table for parameters in Fujimoto Usami formula

F_{fm}/F_{fm0}	a	b	c
0.05	0.188	3.245	0.527
0.1	0.287	3.060	0.573
0.15	0.379	2.894	0.596
0.2	0.476	2.760	0.607
0.25	0.573	2.635	0.615
0.3	0.686	2.505	0.622
0.35	0.805	2.385	0.628
0.4	0.935	2.276	0.634
0.45	1.067	2.165	0.639
0.5	1.220	2.059	0.642
0.55	1.399	1.950	0.645
0.6	1.570	1.838	0.650
0.65	1.751	1.730	0.661
0.7	1.935	1.621	0.683
0.75	2.150	1.510	0.713
0.8	2.178	1.400	0.754
0.85	2.058	1.291	0.839
0.9	1.745	1.175	0.934
0.95	1.291	1.057	0.983
1.0	0.700	0.932	1.013

Figure 7.1: Table from [6] for Eq. 2.14

7.2 Example of formatted Input-File

```

*** 1. DATA FOR OPERATING MODE
      2      1    500 10111      1      1      0      0
      0      1      0      1      1      9      0      0      0
FFFFTF FFFFF FFFFF
*** 2. DATA FOR STANDARD MESH
      1      1      1
T
TFFFF FFFFF
      145    133      0      0
      0.0000E 00  8.2500E 00  1.3000E 01
T
TFFFF
      102    101
      0.0000E 00  6.2500E 00  6.2501E 00
TFFFF
TFFFF
      102    101      0
      0.0000E 00  6.2500E 00  6.2501E 00
FFFFF
      0
FFFFF
      0
*** 3a. DATA FOR NON DEFAULT STANDARD SURFACES, NSTSI=
      10
* outer contour, wall, reflecting, x=0;
      1      1      1
      1      0      0      0      0      2      0      0
SURFMOD_C_300_K
* outer contour, wall, reflecting, x=1.5m
      2      1    145
      1      0      0      0      0      2      0      0
SURFMOD_C_300_K
* outer contour, wall, reflecting, y=0
      3      2      1      1    145      1      1      1    102
      1      0      0      0      0      3      0      0
SURFMOD_C_300_K
* outer contour, wall, reflecting, y=40cm
      4      2    102      1    145    102    102      1    102
      1      0      0      0      0      3      0      0
SURFMOD_C_300_K

```



```

* outer contour, wall, reflecting, z=0
  5      3      1      1    145      1    102      1      1
  1      0      0      0      0      4      0      0
SURFMODE_C_300_K
* outer contour, wall, reflecting, z=40cm
  6      3    102      1    145      1    102    102    102
  1      0      0      0      0      4      0      0
SURFMODE_C_300_K
* inner contour, slitwall, reflecting, x=21cm, 0m<y<9cm, 0cm<z<40cm
  7      1    101    101    101      1    43      1    102
  1      0      0      0      0      2      0      0
SURFMODE_C_300_K
* inner contour, slitwall, reflecting, x=21cm, 11cm<y<40cm, 0cm<z<40cm
  8      1    101    101    101     59    102      1    102
  1      0      0      0      0      2      0      0
SURFMODE_C_300_K
* inner contour, slitwall, reflecting, x=21cm, 0m<y<9cm, 0cm<z<40cm
  9      1    101    101    101     43     59      1     43
  1      0      0      0      0      2      0      0
SURFMODE_C_300_K
* inner contour, slitwall, reflecting, x=21cm, 11cm<y<40cm, 0cm<z<40cm
  10     1    101    101    101     43     59     59    102
  1      0      0      0      0      2      0      0
SURFMODE_C_300_K
*** 3B. DATA FOR ADDITIONAL SURFACES
  2
* additional surface n. 1 crypump
  2.10000E+00 1.00000E+00 1.00000E-05
  1      0      0      0      0      3      0      0      0
+1.29999E+01 0.00001E+00-1.00000E+20+1.29999E+01 6.24999E+00+1.00000E+20
  1      0      0      0
+1.20600E+03-2.60000E-02+0.00000E+00+0.00000E+00+0.00000E+00+0.00000E+00
+1.00000E+00+0.10000E-01+0.00000E+00+1.00000E+00+5.00000E-01+1.00000E+00
* additional surface n. 1 reflecting wrap
-1.00000E+01 1.00000E+00 1.00000E-05
  1      0      0      0      0      3      0      0      0
  6.24999E+00-1.00000E+00 0.00000E+00 0.00000E+00 0.00000E+00 0.00000E+00
  0.00000E+00 0.00000E+00 0.00000E+00 0.00000E+00
-1.92812E+01 0.00000E 00 6.25000E 00+6.25000E 00 0.00000E 00-1.00000E 00
-1.00000E 00 0.00000E 00 0.00000E 00 0.00000E 00
  1      0      0      0
+1.20600E+03-2.60000E-02+0.00000E+00+0.00000E+00+0.00000E+00+0.00000E+00

```

+1.00000E+00+1.00000E 00+0.00000E+00+1.00000E+00+5.00000E-01+1.00000E+00

*** 4. DATA FOR SPECIES SPECIFICATION AND ATOMIC PHYSICS MODULE

* ATOMIC REACTION CARDS NREACI=

1

1 CONST H.2 EL 4 4
-20.9450E 00 0.2500E 00 0.0000E 00 0.0000E 00 0.0000E 00 0.0000E 00
0.0000E 00 0.0000E 00 0.0000E 00 0.0000E 00 0.0000E 00 0.0000E 00

*NEUTRAL ATOMS SPECIES CARDS: NATMI SPECIES ARE CONSIDERED, NATMI=

1

1 H 2 1 1 0 1 -1 2 -1

* NEUTRAL MOLECULES SPECIES CARDS: NMOLI SPECIES ARE CONSIDERED, NMOLI=

1

1 H2(V=?) 4 2 2 0 1 1 0 1
1 214 214 112 01001 000 112
0.0000E 00 0.0000E 00

* TEST ION SPECIES CARDS: NIONI ION SPECIES ARE CONSIDERED, NIONI=

1

1 H2+ 4 2 2 1 0 -1 0 -1 -1

*** 5. DATA FOR PLASMA-BACKGROUND

*BULK ION SPECIES CARDS: NPLSI ION SPECIES ARE CONSIDERED, NPLSI=

2

1 H+ 2 1 1 1 1 -1 2 0
2 H2(B) 4 2 2 0 1 -1 0 0
3 -3 3 3 3 3 0 0 0 0 0 0
1.0000E-02 1.0000E-02 0.0000E 00 0.0000E 00 0.0000E 00 0.0000E 00
1.0000E-02 1.0000E-02 0.0000E 00 0.0000E 00 0.0000E 00 0.0000E 00
1.0000E-02 1.0000E-02 0.0000E 00 0.0000E 00 0.0000E 00 0.0000E 00
1.0000E 01 1.0000E 01 0.0000E 00 0.0000E 00 0.0000E 00 0.0000E 00
1.0000E 01 1.0000E 01 0.0000E 00 0.0000E 00 0.0000E 00 0.0000E 00
0.0000E 00 0.0000E 00 0.0000E 00
0.0000E 00 0.0000E 00 0.0000E 00
0.0000E 00 0.0000E 00 0.0000E 00
0.0000E 00 0.0000E 00 0.0000E 00
1.0000E 00 1.0000E 00 0.0000E 00
1.0000E 00 1.0000E 00 0.0000E 00
0.1000E 00 0.1000E 00 1.0000E 00 1.0000E 00 0.0000E 00

*** 6. DATA FOR GENERAL REFLECTION MODEL

TF

1.0000E 00 1.0000E 00
1.0000E 00
1.0000E 00
1.0000E 00 1.0000E 00

```

1.0000E 00
1.0000E 00 1.0000E 00 0.1000E 00
SURFMOD_C_1150_K
1 00 2 2
1.20600E+03-1.00000E-01 0.00000E+00 0.00000E+00 0.00000E+00 0.00000E+00
1.00000E+00 1.00000E+00 0.00000E+00 1.00000E+00 5.00000E-01 1.00000E+00
1.00000E+00 0.00000E-02 0.00000E+00
SURFMOD_C_300_K
1 00 2 2
1.20600E+03-0.02600E 00 0.00000E+00 0.00000E+00 0.00000E+00 0.00000E+00
1.00000E+00 1.00000E+00 0.00000E+00 1.00000E+00 5.00000E-01 1.00000E+00
1.00000E+00 0.00000E-02 0.00000E+00
*** 7. DATA FOR PRIMARY SOURCES OF NEUTRALS. NSTRAT =
2
1 1
0.0000E 00
* Point Source, 300 K, H2 Molecules, at (x,y,z) = (208, 1.74, 0 ) mid-plane
FFFFF
-1 -1 1 1
1.0000E+02
FTFFF
1
TFFFF
1
1
1.0000E 00 0.0000E 00 0.0000E 00 0.0000E 00 0.0000E 00
0
0.0001E 00 3.0001E+00 3.0001E 00 +1.0000E 00 0.0000E 00 0.0000E 00
0.0260E 00 0.0000E 00
1.0000E 00 9.0000E 01
* Point Source, 300 K, H2 Molecules, at (x,y,z) = (200, 110, 0 )
FFFFF
0 1001 1 1
1.4960E+05
FTFFF
1
TFFFF
1
1
1.0000E 00 0.0000E 00 0.0000E 00 0.0000E 00 0.0000E 00
0
1.5000E 02 -0.9000E+02 0.0000E 00 0.0000E 00 0.0000E 00 0.0000E 00

```

```

-0.0260E 00  0.0000E 00
 1.0000E 00  9.0000E 01
*** 8. ADDITIONAL DATA FOR SPECIFIC ZONES
    0
*** 9. DATA FOR STATISTICS AND NONANALOG METHODS
FFFFF FFFFF FFFFF FFFFF FFFFF FFFFF FFFFF FFFFF FFFFF FFFFF FFFFF FFFFF
    0
    0      0
 1.0000E 03  1.0000E-02  0.0000E 00  7.5000E 02  2.5000E 05  1.0000E-08
 0.2000E 01
*CARDS FOR EMPIRICAL STANDARD DEVIATION, NSIG, NSIGW =
    0      0      0      0      0
    1      2
*** 10. DATA FOR ADDITIONAL VOLUME AND SURFACE AVERAGED TALLIES
    0      0      4      0      0      0
*** 10A.
*** 10B.
*** 10C.
<1,86>/<1,2>
VX, Molecules
H2                      CM/S
<1,90>/<1,2>
VY, Molecules
H2                      CM/S
(<1,62>*<1,62>+<2,62>*<2,62>)*<0.5>
V-POL, Molecules
H2                      CM/S
<1,6>/<1,2>*<0.6667>
Mol. Temperature
H2                      eV
*** 10D.
*** 10E.
*** 11. DATA FOR NUMERICAL AND GRAPHICAL OUTPUT
ftfff tffft fftff ttttt FFFFF ffff ffff
tffff fffff fffff FFFFF
    1
    2      2
    1
    1
TTTTT fftFF FFFFF FFFFF
    1 3019    1
FFFFF

```

```

FFFFF
FFFFF
FFFFF
FFFFF
f radial surfaces      3   1   1   4   4   11 11
f poloidal surfaces    3   1   1   3   4   11 11
f toroidal surfaces    3   1   1   3   4   11 11
    1.5000E 01  1.5000E 01  1.5000E 01  0.0000E 02
    1.5000E 02  5.0000E 01  5.0000E 01  1.5000E 02  5.0000E 01  5.0000E 01
    1.0000E 01  1.0000E 01
      1      0      0      0      0      0      0      0      0      0      1
      0
*** 12. DATA FOR DIAGNOSTIC MODULE. FIRST: CX SPECTRA
      0      0
*** 13. DATA FOR NONLINEAR AND/OR TIME DEP. MODE
      0
*** 14. DATA FOR INTERFACING
      0
      0      0      0

```

7.3 Implemented Code

In the routine */iterate uptbkg.f*, the velocity moments (compare Eq.3.3) are integrated. For the extension, the number of tallies was expanded and the $v_i v_j$ moments (

WTRVXY, WTRVXZ, WTRVXY

) added.

changes in Eirene/iterate/uptbkg.f

CMS for ES-BGK

```

    IBGK=NPBGK
    IUPD1=(IBGK-1)*9+1
    IUPD2=(IBGK-1)*9+2
    IUPD3=(IBGK-1)*9+3
    IUPD4=(IBGK-1)*9+4
    IUPD5=(IBGK-1)*9+5
    IUPD6=(IBGK-1)*9+6
    IUPD7=(IBGK-1)*9+7
    IUPD8=(IBGK-1)*9+8

```

```

IUPD9=(IBGK-1)*9+9
LMETSP(NMTSP+IUPD1)=.TRUE.
LMETSP(NMTSP+IUPD2)=.TRUE.
LMETSP(NMTSP+IUPD3)=.TRUE.
LMETSP(NMTSP+IUPD4)=.TRUE.
LMETSP(NMTSP+IUPD5)=.TRUE.
LMETSP(NMTSP+IUPD6)=.TRUE.
LMETSP(NMTSP+IUPD7)=.TRUE.
LMETSP(NMTSP+IUPD8)=.TRUE.
LMETSP(NMTSP+IUPD9)=.TRUE.
DO 51 I=1,NCOU
DIST=CLPD(I)
WTRV=WV*DIST*VEL
WTRVV=WTRV*VEL
WTRVX=WTRV*VELX
WTRVY=WTRV*VELY
WTRVZ=WTRV*VELZ
WTRVXX=WTRVV*VELX*VELX
WTRVYY=WTRVV*VELY*VELY
WTRVZZ=WTRVV*VELZ*VELZ
WTRVXY=WTRVV*VELX*VELY
WTRVXZ=WTRVV*VELX*VELZ
WTRVYZ=WTRVV*VELY*VELZ
IRD=NRCELL+NUPC(I)*NR1P2+NBLCKA
BGKV(IUPD1,IRD)=BGKV(IUPD1,IRD)+WTRVX
BGKV(IUPD2,IRD)=BGKV(IUPD2,IRD)+WTRVY
BGKV(IUPD3,IRD)=BGKV(IUPD3,IRD)+WTRVZ
BGKV(IUPD4,IRD)=BGKV(IUPD4,IRD)+WTRVXX
BGKV(IUPD5,IRD)=BGKV(IUPD5,IRD)+WTRVYY
BGKV(IUPD6,IRD)=BGKV(IUPD6,IRD)+WTRVZZ
BGKV(IUPD7,IRD)=BGKV(IUPD7,IRD)+WTRVXY
BGKV(IUPD8,IRD)=BGKV(IUPD8,IRD)+WTRVXZ
BGKV(IUPD9,IRD)=BGKV(IUPD9,IRD)+WTRVYZ

```

CMS END

In the */iterate/modbgk.f* routine, the moments were calculated to the pressure-tensor and finally transformed according to Eq. 3.34.

Changes in Eirene/iterate/modbgk.f

```

CMS - pressure tensor
      PRXX(IRAD)=BGKV(IUP4,IRAD)-VXIN(IPLSV,IRAD)**2*
      PDEN(IRAD)
      PRYY(IRAD)=BGKV(IUP5,IRAD)-VYIN(IPLSV,IRAD)**2*
      PDEN(IRAD)
      PRZZ(IRAD)=BGKV(IUP6,IRAD)-VYIN(IPLSV,IRAD)**2*
      PDEN(IRAD)
      PRXY(IRAD)=BGKV(IUP7,IRAD)-VXIN(IPLSV,IRAD)*
      VYIN(IPLSV,IRAD)*PDEN(IRAD)
      PRXZ(IRAD)=BGKV(IUP8,IRAD)-VXIN(IPLSV,IRAD)*
      VZIN(IPLSV,IRAD)*PDEN(IRAD)
      PRYZ(IRAD)=BGKV(IUP9,IRAD)-VYIN(IPLSV,IRAD)*
      VZIN(IPLSV,IRAD)*PDEN(IRAD)

CMS END

C NEW N
      DIIN(IPLS,IRAD)=PDEN(IRAD)
      RRN=RRN+PDEN(IRAD)*VOL(IRAD)
C      RRM=?
      RRE=RRE+EDEN(IRAD)*VOL(IRAD)

CMS
c ES transformation matrix
c TRCL(1,IRAD)=lambda_11, TRCL(2,IRAD)=lambda_21, TRCL(3,IRAD)=lambda_22,
c TRCL(4,IRAD)=lambda_31, TRCL(5,IRAD)=lambda_32, TRCL(6,IRAD)=lambda_33
c ESCF=ES-coefficient=-1/2;
c TRCL in cm**2/s**2

c      TRCL(1,IRAD)=(1-ESCF)*TIIN(IPLSTI,IRAD)/FACT1/2+
c      .      ESCF*PRXX(IRAD)/DIIN(IPLS,IRAD)+EPS60
      TRCL(2,IRAD)=ESCF*PRXY(IRAD)/(DIIN(IPLS,IRAD))
c      TRCL(3,IRAD)=(1-ESCF)*TIIN(IPLSTI,IRAD)/FACT1/2+
c      .      ESCF*PRYY(IRAD)/DIIN(IPLS,IRAD)+EPS60
      TRCL(4,IRAD)=ESCF*PRXZ(IRAD)/(DIIN(IPLS,IRAD))
      TRCL(5,IRAD)=ESCF*PRYZ(IRAD)/(DIIN(IPLS,IRAD))
c      TRCL(6,IRAD)=(1-ESCF)*TIIN(IPLSTI,IRAD)/FACT1/2+
c      .      ESCF*PRZZ(IRAD)/DIIN(IPLS,IRAD)+EPS60
      TRCL(1,IRAD)=TIIN(IPLSTI,IRAD)/FACT1/2
      TRCL(3,IRAD)=TIIN(IPLSTI,IRAD)/FACT1/2
      TRCL(6,IRAD)=TIIN(IPLSTI,IRAD)/FACT1/2

```

```

c Transformation of transformation matrix:  $X_{ij} = \sum(a_{ik} * a_{jk}) = \lambda_{ij}$  ;  $X_{ij}$ 
c dreiecksmatrix;
c coefficient ADIN(1,IRAD)=a_11; ADIN(2,IRAD)=a_21; ADIN(3,IRAD)=a_22; etc analog TRCL
c to be sent to veloel.f; used to transform samples from maxwellian, to samples from
c ADIN in cm/s

```

```

        ADIN(1,IRAD)=SQRT(TRCL(1,IRAD))
        ADIN(2,IRAD)=TRCL(2,IRAD)/(ADIN(1,IRAD))
        ADIN(3,IRAD)=SQRT(TRCL(3,IRAD)-ADIN(2,IRAD)**2)
        ADIN(4,IRAD)=TRCL(4,IRAD)/(ADIN(1,IRAD))
        ADIN(5,IRAD)=(TRCL(5,IRAD)-ADIN(4,IRAD)*
.         ADIN(2,IRAD))/ADIN(3,IRAD)
        ADIN(6,IRAD)=SQRT(TRCL(6,IRAD)-ADIN(4,IRAD)**2-
.         ADIN(5,IRAD)**2)

```

```

c  if ADIN NaN set 0
    IF (ADIN(1,IRAD) .NE. ADIN(1,IRAD)) THEN
        ADIN(1,IRAD)=0
        ADIN(2,IRAD)=0
        ADIN(3,IRAD)=0
        ADIN(4,IRAD)=0
        ADIN(5,IRAD)=0
        ADIN(6,IRAD)=0
    ELSE IF (ADIN(2,IRAD) .NE. ADIN(2,IRAD)) THEN
        ADIN(1,IRAD)=0
        ADIN(2,IRAD)=0
        ADIN(3,IRAD)=0
        ADIN(4,IRAD)=0
        ADIN(5,IRAD)=0
        ADIN(6,IRAD)=0
    ELSE IF (ADIN(3,IRAD) .NE. ADIN(3,IRAD)) THEN
        ADIN(1,IRAD)=0
        ADIN(2,IRAD)=0
        ADIN(3,IRAD)=0
        ADIN(4,IRAD)=0
        ADIN(5,IRAD)=0
        ADIN(6,IRAD)=0
    ELSE IF (ADIN(4,IRAD) .NE. ADIN(4,IRAD)) THEN
        ADIN(1,IRAD)=0
        ADIN(2,IRAD)=0

```



```

ADIN(3,IRAD)=0
ADIN(4,IRAD)=0
ADIN(5,IRAD)=0
ADIN(6,IRAD)=0
ELSE IF (ADIN(5,IRAD) .NE. ADIN(5,IRAD)) THEN
ADIN(1,IRAD)=0
ADIN(2,IRAD)=0
ADIN(3,IRAD)=0
ADIN(4,IRAD)=0
ADIN(5,IRAD)=0
ADIN(6,IRAD)=0
ELSE IF (ADIN(6,IRAD) .NE. ADIN(6,IRAD)) THEN
ADIN(1,IRAD)=0
ADIN(2,IRAD)=0
ADIN(3,IRAD)=0
ADIN(4,IRAD)=0
ADIN(5,IRAD)=0
ADIN(6,IRAD)=0
END IF

```

CMS END

In the *particle-tracing/veloel.f* the Samples from a 3-D Maxwell distribution are transformed by the transformation coefficient a_{ij} in accordance with Eq. [3.36](#).

```

%changes in Eirene/particle-tracing/veloel.f
C  SAMPLE FROM 3D MAXWELLIAN
    VXN=FG1(INIV2)
    VYN=FG2(INIV2)
    VZN=FG3(INIV2)
    INIV2=INIV2-1

CMS - transform 3D-gauss samples with a_ij(ES)
c to velocity relative to background

```

```

c check if ADIN = 0
  TIILIM=ADIN(1,K)+ADIN(2,K)+ADIN(3,K)
  .+ADIN(4,K)+ADIN(5,K)+ADIN(6,K)
  IF (TIILIM .NE. 0) THEN

    CHI1=VXN
    CHI2=VYN
    CHI3=VZN

    VXN=(ADIN(1,K)*CHI1)
    VYN=(ADIN(2,K)*CHI1+ADIN(3,K)*CHI2)
    VZN=(ADIN(4,K)*CHI1+ADIN(5,K)*CHI2+ADIN(6,K)*
    .      CHI3)
c normalize with respect to thermal velocity
  NORMALIZE=SQRT(VXN**2+VYN**2+VZN**2)/SQRT(CHI1**2+CHI2**2+CHI3**2)

  VXN=VXN/NORMALIZE
  VYN=VYN/NORMALIZE
  VZN=VZN/NORMALIZE

  END IF
CMS END

```

Bibliography

- [1] Script from IPP Summer University for Plasma Physics, Greifswald, 2009.
- [2] Wojciech Fundamenski. *Power Exhaust in Fusion Plasmas*. Camebridge University Press, 2010.
- [3] M. Keilhacker and ASDEX Team. The asdex divertor tokamak. *Nuclear Fusion*, 1985.
- [4] Marco Wischmeier. *Simulating Divertor Detachment in the TCV and JET tokamaks*. PhD thesis, Ecole Polytechnique Federal de Lausanne, 2004.
- [5] D.Reiter. *The EIRENE Code User Manual*, 2009.
- [6] Tetsuo Fujimoto, Masaru Usami. Rarefied Gas Flow Through a Circular Orifice and Short Tubes. *Journal of Fluids Engineering*, 106, 1984.
- [7] Felix Sharipov, Dalton V. Kozak. Rarefied gas flow through a thin slit into vacuum simulated by the Monte Carlo method over the whole range of th Knudsen number. *American Vacuum Society*, 2009.
- [8] A.K.Sreekanth. Transition flow through short circular tubes. *The Physics of Fluids*, 1965.
- [9] S.Varoutis, D.Valougeorgis, F.Sharipov. Simulation of gas flow through tubes of finite length over the whole range of rarefaction for various pressure drops ratios. *Journal of Vacuum Science and Technology*, 2009.
- [10] Michail A. Gallis, John R. Torczynski. An improved BGK-Type Collision-Term Model for Direct Simulation Monte Carlo DSMC Method. *Physics of Fluids*, 2000.
- [11] J.M. Lafferty. *Foundations of Vacuum Science*. John Wiley and Sons, Inc., 1998.
- [12] Martin Knudsen. Die Gesetze der Molekularstroemung und der inneren Reibungsstroemung der Gase durch Roehren. *Annalen der Physik*, 333, 1909.
- [13] Felix Sharipov and Vladimir Seleznev. Data on Internal Rarefied Gas Flows. *American Institute of Physics and American Chemical Society*, 1998.

- [14] Vladislav Kotov, Detlev Reiter, Andrey S. Kukushkin. Numerical study of the ITER divertor plasma with the B2-EIRENE code package. Technical report, Forschungszentrum Juelich GmbH, 2007.
- [15] S.Varoutis, D. Valougeorgis, F. Sharipov. Simulation of gas flow through tubes of finite length over the whole range of rarefaction for various pressure drop ratios. *Journal of Vacuum Science and Technology A*, 27, 2009.
- [16] Felix Sharipov and Dalton V. Kozak. Rarefied gas flow through a thin slit into vacuum simulated by the Monte Carlo method over the whole range of the Knudsen number. *American Vacuum Society*, 27, 2009.
- [17] Harald Lesch, G.T. Birk, Hartmut Zohm, Hanna Kotarba. T 6 - Theoretische Hydrodynamik, 2006. Lecture Script given at LMU Munich.
- [18] Lester Lees. Kinetic Theory Description of Rarefied Gas Flow. *Journal of the Society for Industrial and Applied Mathematics*, 13, 1965.
- [19] D.Reiter, Chr. May, M. Baelmans, P.Boerner. Non-linear effects on neutral gas transport in divertors. *Journal of Nuclear Materials*, 1997.
- [20] Scott L. Thompson, William R. Owens. A survey of flow at low pressures. *Vacuum - Elsevier*, 1974.
- [21] P.Clausing. Ueber die Stroemung sehr verduennter Gase durch Roehren von beliebiger Laenge. *Annalen der Physik*, 404, 1932.
- [22] M.v. Smoluchowski. Zur kinetischen Theorie der Transpiration und Diffusion verduennter Gase. *Annalen der Physik*, 338, 1910.
- [23] W.Steckelmacher. Knudsen flow 75 years on: the current state of the art for flow of rarefied gases in tubes and systems. *Reports on Progress in Physics*, 49, 1986.
- [24] W. Steckelmacher. The effect of cross-sectional shape on the molecular flow in long tubes. *Vacuum - Elsevier*, 28, 1978.
- [25] V. Varoutis, V. Hauer, C. Day, S. Pantazis, D. Valougeorgis. Experimental investigation in flow configurations related to the vacuum systems of fusion reactors. *Fusion Engineering and Design*, 85, 2010.
- [26] L.Marino. Experiments on rarefied gas flow. *Microfluidics and Nanofluidics*, 2009.
- [27] T.C Lilly, S.F Gimelsheim, A.D. Ketsdever, G.N. Markelov. Measurement and computations of mass flow and momentum flux through short tubes in rarefied gases. *Physics of Fluids*, 18, 2006.

- [28] M.A. Gallis, J.r. Torczynski, D.J. Rader. Molecular gas dynamics observations of chapman-enskog behavior and departures ferefrom in nonequilibrium gases. *Physical Review*, 69, 2004.
- [29] G.A. Bird, M.A. Gallis, J.R. Torczynski, D.J. Rader. Accuracy and efficiency of the sophisticated direct simulation monte carlo algorithm for simulating non-contiunuum gas flows. *Physics of Fluids*, 21, 2009.
- [30] Toshiyuki Doi. Numerical analysis of the poiseuile flow and the thermal transpiration of a rarefied gas through a pipe with a rectangular cross section based on the linearized boltzmann equation for a hard sphere molecular gas. *Journal of Vacuum Science and Technology*, 2010.
- [31] A.Roth. *Vacuum Technology*. Elsevier Science, 1990.
- [32] Hans W. Liepmann. Gaskinetics and gasdynamics of orifice flow. *Journal of Fluid Mechanics*, 1961.
- [33] F.Schwabl. *Statistische Mechanik*. Springer-Verlag, 1999.
- [34] Dimitris Valougeorgis. Solution of vacuum flows via kinetic theory. 51st IU-VSTA Workshop on Modern Problems and Capability of Vacuum Gas Dynamics, 2007.
- [35] Phoolan Prasad. P.L. Bhatnagar and the BGK Model, 2007. 19th P.L. Bhatnagar Memorial Award Lecture 2006.
- [36] Lowell H. Holway, Jr. New Statistical Models for Kinetic Theory: Methods of Construction. *The Physics of Fluids*, 9, 1966.
- [37] W.G. Vincenti, C.H. Kruger, Jr. *Introduction to Physical Gas Dynamics*. John Wiley and Sons, Inc., 1965.
- [38] Pierre Andries, Patrick Le Tallec, Jean-Philippe Perlat, Benoit Perthame. The Gaussian-BGK Model of Boltzmann Equation with Small Prandtl Number. *European Journal of Mechanics -B/Fluids*, 19, 2000.
- [39] <http://www.eirene.de>. EIRENE homepage.
- [40] Saul Dushman. *Scientific Foundations of Vacuum Technique*. John Wiley and Sons, Inc., 1966.
- [41] M.D. Boekmann D.J. Santeler. Molecular flow transmission probabilities of rectangular tubes. *Journal of Vacuum Science and Technology*, 9, 1991.

Acknowledgements

I first like to thank Prof. Hartmut Zohm for giving me the the opportunity to undertake my Diploma thesis at IPP, Garching and whose uplifting comments motivated me for my work.

Secondly I would like to express my deepest gratitude to Dr.Andrea Scarabosio for his patient supervision and overall support. I could learn many things from him and i am very grateful for the time and effort he spend on guiding me through this thesis. I also want to thank him for arranging for me to carry out part of my work for this thesis at Forschungszentrum Jülich, which was quite an exciting experience.

I would also like to thank Dr.Detelv Reiter for suggesting to write the BGKES extension in Jüelich and for taking sincere interest in my work.

I want to thank Dr.Valdislav Kotov and Petra Boerner in particular for their support and time. I am incredibly thankful for the help I received with EIRENE and for making me feel welcome.

I also want to thank Dr.Alberto Bottino, Dr. Vitus Mertens, Dr. Albrecht Hermann and Fr. Gabriella Daube as well as the whole staff of IPP, where I always felt comfortable.

I especially want to thank my friends Korbinian Paul, Nicolette Helling and Moritz Schneider, for proof-reading this thesis and for giving me good advice.

Last but not least I want to thank my family and my friends for putting up with my busy schedule and for being there for me, when I need them.

Erklärung

des Diplomanden

Simon, Marek Sebastian

Mit der Abgabe der Diplomarbeit erkläre ich, dass ich die Arbeit selbstständig verfasst und keine anderen als die angegebenen Quellen und Hilfsmittel benutzt sowie Zitate kenntlich gemacht habe.

München, den May 31, 2011

Unterschrift